frontiers in Earth Science

ORIGINAL RESEARCH
published: 30 June 2020
doi: 10.3389/feart.2020.00212

Petrogenesis of the Kanker Granites From the Bastar Craton: Implications for Crustal Growth and Evolution During the Archean-Proterozoic Transition

Ajay Dev Asokan[1], *R. Elangovan*[1], *Neeraj Vishwakarma*[2], *K. R. Hari*[3] *and M. Ram Mohan*[1]*

[1] CSIR-National Geophysical Research Institute, Hyderabad, India, [2] Department of Applied Geology, National Institute of Technology, Raipur, India, [3] Department of Geology and Water Resources Management, Pt. Ravishankar Shukla University, Raipur, India

Archean-Proterozoic boundary represents a significant transitional phase in the Earth's history. Bastar Craton is one of the major Archean cratons in the Indian subcontinent with voluminous granites, supracrustal rocks, and tectonic belts. Malanjkhand, Dongargarh, and Kanker are the three major granitic plutons emplaced during the Archean-Proterozoic transition in the Bastar Craton, and this study is confined to the granites of Kanker pluton. Based on geochemical systematics, the Kanker granites are classified into sanukitoids, biotite and two-mica granites, and hybrid granites. The compositional diversity of the Kanker granites is attributed to two end-member sources, i.e., the enriched mantle and an older felsic crust, and the interactions between them. The sanukitoids were derived from an enriched mantle source that was metasomatized by the subducted sediments. Heat supplied by the sanukitoid magmas induced the crustal melting to form the biotite and two-mica granites. The interaction between these two mutually end-member sources, i.e., the enriched mantle and an older felsic crust, resulted in the formation of hybrid granites. The evolution of the Kanker granites can be accounted for a transitional geodynamic environment, involving subduction, and collisional tectonics during the Archean-Proterozoic transition.

Keywords: sanukitoids, biotite and two-mica granites, Archean-Proterozoic transition, subduction and collisional tectonics, Bastar Craton

OPEN ACCESS

Edited by:
Steven W. Denyszyn, University of Western Australia, Australia

Reviewed by:
Marcos Garcia-Arias, University of Los Andes, Colombia
Xiaoping Xia, Chinese Academy of Sciences, China

***Correspondence:**
M. Ram Mohan
rammohan@ngri.res.in

Specialty section:
This article was submitted to Petrology, a section of the journal Frontiers in Earth Science

Received: *11 March 2020*
Accepted: *20 May 2020*
Published: *30 June 2020*

Citation:
Asokan AD, Elangovan R, Vishwakarma N, Hari KR and Ram Mohan M (2020) Petrogenesis of the Kanker Granites From the Bastar Craton: Implications for Crustal Growth and Evolution During the Archean-Proterozoic Transition. Front. Earth Sci. 8:212. doi: 10.3389/feart.2020.00212

INTRODUCTION

The Archean-Proterozoic boundary witnessed critical changes in the Earth's history, such as the increase in the crustal thickness, decrease in the rate of continental crustal growth, oxygenation of the atmosphere, widespread occurrences of plate tectonic indicators and the formation of supercontinental assemblages (Durrheim and Mooney, 1991; Condie and Kröner, 2008; Keller and Schoene, 2012; Cawood et al., 2013; Lee et al., 2016). Most of these changes are linked to the secular cooling of the Earth's mantle that has utmost implications on the geological processes and is related to the onset of present-day plate tectonics (Sizova et al., 2010; Keller and Schoene, 2012). Granitic magmatism has been recorded as early as Hadean, in the Acasta Gneissic Complex (Reimink et al., 2016) and continued into the Miocene (Hopkinson et al., 2017).

Granitic rocks, unique to the planet Earth, provide vital clues on the formation and evolution of the continental crust (Cawood et al., 2013). Formation of granitic rocks can occur by two different mechanisms, i.e., melting and differentiation of basaltic rock and/or by the melting of the pre-existing crustal rocks (Moyen et al., 2017). The transition from a stagnant lid tectonic regime to present-day plate tectonics is believed to have initiated by 3.0 Ga and became prominent by the end of the Archean (Dhuime et al., 2012; Keller and Schoene, 2012). The global transition in the nature and style of plate tectonic processes is well-reflected and resulted in the compositional diversification of the Neoarchean granitoids (Moyen et al., 2003; Laurent et al., 2014). Based on the source and petrogenetic mechanism, the Neoarchean granitoids have been classified into Tonalite Trondhjemite Granodiorites (TTGs), sanukitoids s.l., biotite and two-mica granites and hybrid granites (Laurent et al., 2014). The TTGs are sourced from the partial melting of metabasalts, sanukitoids are derived from an enriched mantle, and the biotite and two-mica granites are purely crustal-derived. The hybrid granites are formed by variable interaction between the three above-mentioned granitic melts (Laurent et al., 2014).

There has been widespread granitic magmatism in the Indian shield, as seen in the Aravalli, Bundelkhand, Dharwar, and Bastar cratons during the Archean-Proterozoic boundary (Jayananda et al., 2020). The Bastar Craton (**Figure 1**), with abundant Archean-Proterozoic supracrustals and granitoids, hold critical clues reflecting the significant changes that occurred during this period (Khanna et al., 2019; Mondal et al., 2019; Santosh et al., 2020). Malanjkhand, Dongargarh, and Kanker are the three major granitic plutons emplaced during the Archean-Proterozoic transition in the Bastar Craton. Based on the whole rock geochemistry, this study intends to characterize the granites of Kanker pluton and to provide new insights on the petrogenetic evolution of these granites. The results have implications on the crustal growth during the Archean-Proterozoic transition, vis-à-vis, the evolutionary history of the Bastar Craton.

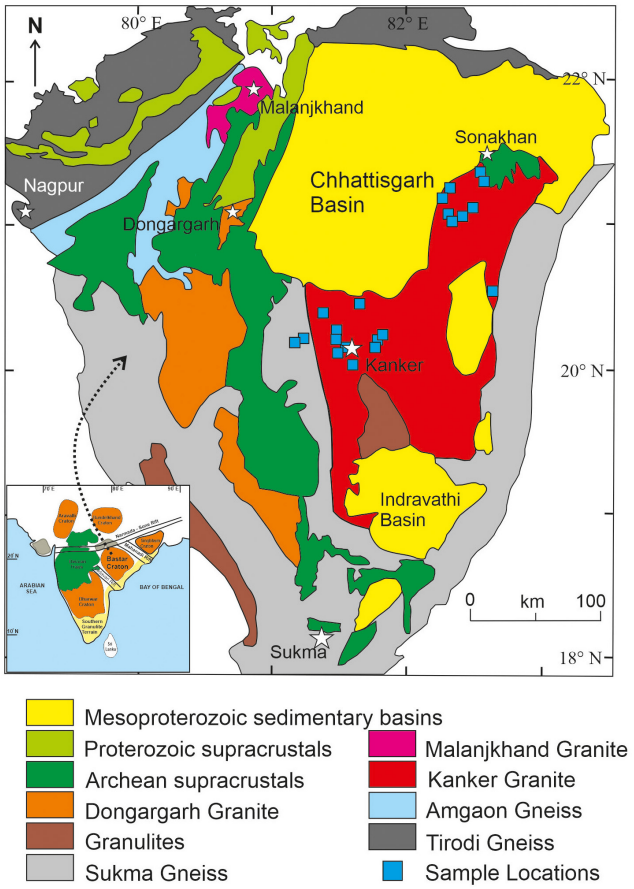

FIGURE 1 | Generalized geological map of the Bastar Craton, with the sample locations (modified after Mohanty, 2015). Inset map of Peninsular India, to show the major cratonic blocks.

GEOLOGY OF THE BASTAR CRATON

The Indian Shield is an amalgamation of cratonic blocks, namely Dharwar, Singhbhum, Bastar, Aravalli, and Bundelkhand cratons separated by Proterozoic mobile belts. The Bastar Craton of central India is bound by the Mahanadi Rift and the Eastern Ghats in the east, the Central Indian Tectonic Zone (CITZ) toward the west, and the Godavari rift in the southeast (**Figure 1**). The Eastern Ghats Mobile Belt forms the southeast boundary of this craton. The craton records evidence for crustal growth as early as Paleoarchean (Sarkar et al., 1993; Ghosh, 2004; Rajesh et al., 2009). The Sukma gneissic complex is considered as the basement of the Bastar Craton (Ramakrishnan, 1990). The basement gneisses are best exposed along the southern part of this craton. Tonalites forming the Sukma gneissic complex yielded a U-Pb zircon age of 3561 ± 11 Ma (Ghosh, 2004). The potassic granites associated with these TTGs were also emplaced during the Paleoarchean (Rajesh et al., 2009). The Sukma Group overlies the Paleoarchean basement gneisses and constitutes mafic-ultramafics, BIFs, para-amphibolites, and quartzites (Mohanty, 2015). The CITZ divides the Sukma gneissic complex into the southern Amgaon gneiss and the northern Tirodi gneiss. The ages of Amgaon gneiss ranges from 2378 to 3396 Ma (Sm-Nd ages, Ahmad et al., 2009). The Tirodi biotite gneisses yielded an emplacement age of 1618 ± 8 Ma (U-Pb zircon age, Bhowmik et al., 2011).

The Bengpal Group overlies the older Sukma Group with a basal unconformity. The major rock types of the Bengpal Group are quartzites, amphibolites, BIFs, and interlayered metabasalts with quartzites (Mohanty, 2015). Neoarchean boninite-like rocks and siliceous high magnesium basalts (SHMBs) were reported from the Bengpal Group (Srivastava et al., 2004) and the Neoarchean Sonakhan Greenstone Belt (SGB) (Manu Prasanth et al., 2018). The younger supracrustals of the craton comprise metavolcanics, metasedimentary sequences and BIFs that occur as enclaves, as well as linear belts. The Dongargarh, Sakoli and Sausar are the prominent supracrustal belts in this craton (Meert et al., 2010). The Dongargarh Supergroup, constituting the supracrustals and granites, is further divided into Nandgaon

and Khairagarh groups being separated by the Dongargarh granite (Deshpande et al., 1990). The Nandgaon Group consists of Bijli rhyolite and Pitapani basalts and andesites, whereas the Khairagarh Group consists of basalts interlayered with sandstone and arenites (Khanna et al., 2019). The volcanic rocks of the Dongargarh Supergroup, referred to as the Kotri-Dongargarh Mobile Belt (KDMB), are interpreted to have erupted by ∼2.5 Ga (Asthana et al., 2016; Manikyamba et al., 2016; Khanna et al., 2019), and are considered to have evolved in an arc setting (Asthana et al., 2018).

The Neoarchean orogenic events in the craton are marked by the formation of migmatites from the basement granitoids (Roy et al., 2006). The Neoarchean-early Paleoproterozoic granitic magmatism is reported in the form of three major plutons, namely, Dongargarh, Kanker, and Malanjkhand granites. The I-type Malanjkhand granite hosts a world-class copper-molybdenum deposit and was emplaced around 2478 Ma (Panigrahi et al., 2004). There is no consensus on the tectonic setting of the Malanjkhand granite and the origin of mineralization (Stein et al., 2004; Pandit and Panigrahi, 2012; Asthana et al., 2016). The Dongargarh granite is a composite pluton, with both I- and A-type affinity (Narayana et al., 2000) and is considered to have evolved in a continental rift setting (Pandit and Panigrahi, 2012; Manikyamba et al., 2016). Dongargarh granite has yielded a U-Pb zircon age of 2485 ± 6.5 Ma and is considered to be coeval with the 2.48 Ga Kanker granites (Sarkar et al., 1993; Bickford et al., 2014). In a recent study (Santosh et al., 2020), the Bastar Craton is divided into Western Bastar, and Eastern Bastar cratons, sutured by the N-S directed collisional Central Bastar Orogen. Several dyke swarms of the craton exhibit NW–SE trend, which is parallel to the Godavari Rift (Meert et al., 2010). French et al. (2008) has reported the U-Pb baddeleyite age of 1891.1 ± 0.9 Ma and U-Pb zircon age of 1883 ± 1.4 Ma for dolerite dykes from the southern part of this craton. Meso-Neoproterozoic Chhattisgarh, Khariar, and Indravathi basins overlie on the Kanker granite (Bickford et al., 2014).

FIELD RELATIONSHIPS AND PETROGRAPHY

We present the field, petrographic, and whole-rock geochemical studies for the unclassified granites representing the Kanker granitic pluton from the central part of the Bastar Craton. The Kanker granite is a composite granitic pluton with at least three phases of granites. Porphyritic feldspar megacrystic granites are the most common variety, varying from pink to gray in color (**Figures 2A,B**). Apart from the porphyritic granitoids, leucogranites and anatectic granites are also present (**Figures 2C,D**). Microgranular enclaves (MEs), and mafic synplutonic dykes were observed at several places (**Figure 2E**). The granite variants mostly display sharp contacts (**Figure 2F**). Elangovan et al. (2017, 2020), have found that the mafic and felsic magmatism were coeval. These granites are variably deformed at places and form granitic gneisses. Pegmatites, aplite, and epidote veins are found intruding into these granites. The pegmatite veins contain large alkali feldspar crystals (2–6 cm in length) with perfect twins and perthite exsolution along with tourmaline, titanite, and allanite. In general, these granites are oriented along NW-SE direction.

Based on the mineral assemblages, the Kanker granites can be divided into two, namely, biotite, and two-mica granite and hornblende biotite granite. The biotite and two-mica granites display inequigranular texture with twinned alkali feldspars showing the perthitic exsolution. The essential minerals that constitute biotite and two-mica granites are alkali feldspar, plagioclase, and quartz, with biotite and muscovite forming the accessory phases (**Figures 3A,B**). The alkali feldspars contain inclusions of plagioclase, quartz, and biotite. Perthite unmixing is common from both microcline and orthoclase. Mafic minerals such as hornblende, titanite, and opaques are nearly absent in these granites. Sericitization of plagioclase and chloritization of biotite are common (**Figure 3C**).

The Hornblende biotite granites exhibit hypidiomorphic texture with plagioclase, alkali feldspar, and quartz as the essential minerals. Titanite, epidote, opaques, apatite, zircon, and allanite forms the accessory phases (**Figure 3D**). The plagioclase feldspars are euhedral and display kink in their twins (**Figure 3D**). The alkali feldspars, which are subhedral to anhedral, exhibit perthitic exsolution. A few crystals of hornblende exhibit twinning, and most of them are chloritized, along with biotite. Apatites are mostly prismatic, though few acicular ones are also observed. Allanite crystals are well-zoned and elongated (**Figure 3E**). Primary epidotes are rarely seen, while the secondary epidotes are fairly common. Titanite grains are mostly associated with biotite and hornblende, and they vary from euhedral wedge to irregular in shape (**Figure 3F**).

ANALYTICAL TECHNIQUES

The granitoid samples weighing more than ∼3 kg were collected from fresh outcrops and working quarries. For geochemical analysis, the samples were crushed to fine powders of size <250 mesh sieve. The geochemical analysis was carried out using in-house facilities at CSIR-National Geophysical Research Institute, Hyderabad. The major elements of the studied samples are analyzed using XRF (Phillips Axios mAX4), following the pressed pellet sample preparation technique. USGS standard reference material G-2 was used as the standard. The details of instrument calibration, data acquisition, accuracy, and detection limits are provided in Krishna et al. (2016). The trace elements were analyzed using AttoM HR-ICP-MS (Nu Instruments, UK), following the closed digestion sample preparation technique. About 50 mg of finely powdered samples were taken in Savillex® vials to which 10 ml of the acid mixture containing HF and HNO_3 mixed in 7:3 ratio was added. After heating these vials for 48 h at 150°C to obtain a clear solution, 1 ml of perchloric acid was added, and the samples were heated to dryness. Twenty ml of a freshly prepared acid mixture containing HF and Millipore water in a 1:1 ratio was added to the vials and heated for nearly 1 h at 80°C. On cooling, the sample solution was transferred to 250 ml conical flasks, and 5 ml of 1 ppm Rh

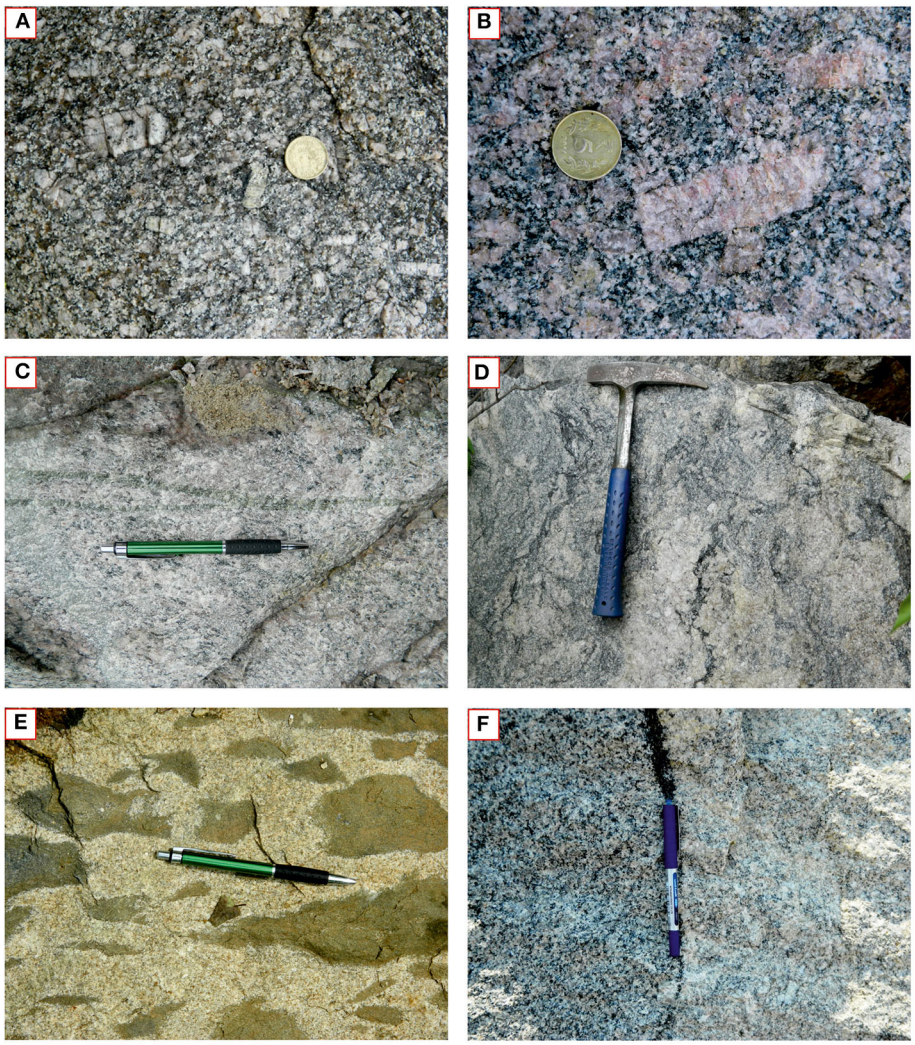

FIGURE 2 | Field photographs of different granite types from Kanker **(A)** Gray porphyritic granite with feldspar phenocryst. **(B)** Pink porphyritic granite with alkali feldspar phenocrysts. Both these granitoids are high in mafic minerals. **(C)** Medium- to coarse-grained leucogranite being intruded by an epidote vein. **(D)** Gray medium- to coarse-grained anatectic granite. **(E)** Medium to coarse- grained gray granite with abundant Magmatic Enclaves (MEs). **(F)** Two granitoid variants that differ in their mafic mineral contents, demarcated by a sharp boundary of biotite aggregates.

was added as an internal standard. The sample solution was initially diluted to 250 ml, followed by a 50 ml dilution, to achieve an optimal Total Dissolved Solid (TDS) level. Along with the samples, blank solutions and standards JG-1a and G-2 were also used. The data accuracy was monitored using certified reference materials (JG-1a and G-2), and the instrument sensitivity and stability was checked with Rh. The contamination was monitored using the blank solutions. The details of the sample digestion method, instrumental parameters, data acquisition, and quality are referred from Satyanarayanan et al. (2018).

RESULTS

Geochemistry

The whole-rock major and trace elemental data for 39 samples representing the Kanker granites are presented in **Table 1**. Based on the normative mineralogy, the Kanker granites are mostly granites with few granodiorites and quartz monzonite (**Figure 4A**). Considering the compositional variability of these granites, in conjunction with the variations in mineral assemblages, these granites are divided into sanukitoids, biotite and two-mica granites and hybrid granites (as dispositioned in **Figure 4B**). This classification scheme enables us to characterize these rocks for the petrogenetic evolution and sources, apart from being consistent with the global adaptability of Neoarchean granitoids (Laurent et al., 2014).

Sanukitoids

Based on the normative mineralogy, the sanukitoids of the Kanker are granites, granodiorites and quartz monzonites (**Figure 4A**) with a high content of ferromagnesian elements (Fe_2O_3, MgO, MnO and TiO_2, FMMT >5 wt.%) (**Figure 4B**).

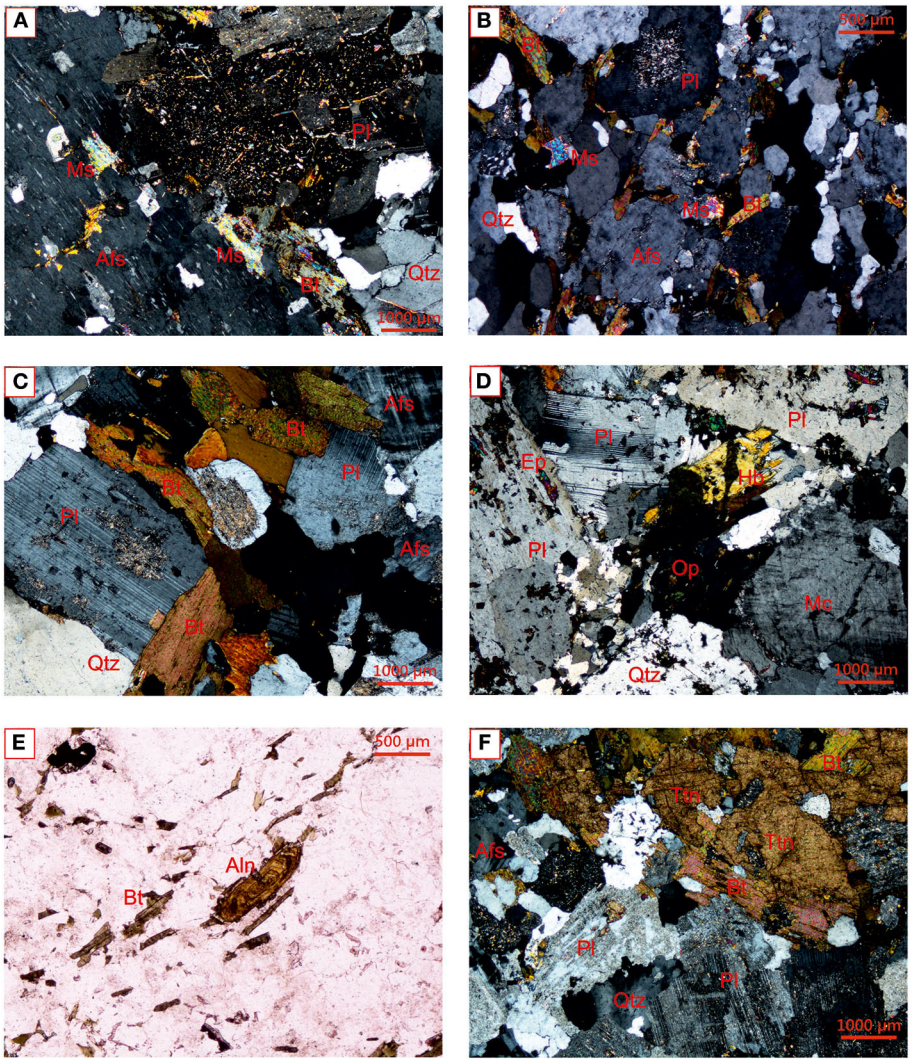

FIGURE 3 | Representative photomicrographs of Kanker granites **(A)** Biotite and two-mica granite with sericitized plagioclase, alkali feldspar with plagioclase and quartz inclusions, chloritized biotite, and muscovite. **(B)** Biotite and two-mica granite with plagioclase, alkali feldspar, quartz, biotite and muscovite. Quartz exhibits sub-grain formation. **(C)** Biotite granite with plagioclase, alkali feldspar, quartz and biotite. The alteration of plagioclase is limited to their cores and possess growth twins. **(D)** Hornblende biotite granite with hornblende, plagioclase, microcline, quartz and opaques. Plagioclase possesses deformational kinks. **(E)** An elongated zoned allanite grain observed in the biotite granite. **(F)** Biotite granite with large titanite grains associated with biotite, extensively sericitized plagioclase, alkali feldspar and recrystallized quartz. The mineral abbreviations in the figure are Ms, Muscovite; Afs, Alkali feldspar; Bt, Biotite; Pl, Plagioclase; Qtz, Quartz; Ep, Epidote; Op, Opaque; Mc, Microcline; Ttn, Titanite; Aln, Allanite.

Their silica and alumina compositions range between 63 and 69 wt.% and 12 to 16 wt.%, respectively (**Table 1**). These granites are essentially potassic (K_2O = 3.4–5.4 wt.%) with metaluminous affinity (A/CNK <1) and belongs to high-K calc-alkaline to shoshonitic series (**Figures 5A,B**). The sanukitoids have Mg number (Mg#) as high as 66 with an average of 46 (**Figure 5C**). On the Harker variation diagrams, these sanukitoids exhibit a negative trend against the major elements, with marked enrichment in the ferromagnesian elements (**Figures 5D–F**).

The sanukitoids have higher compositions of transition elements (**Table 1**). These rocks have low Rb (avg. 168 ppm) and high Sr (avg. 310 ppm) compositions, leading to extremely low Rb/Sr ratios (avg. Rb/Sr = 0.54). On the chondrite normalized rare earth element (REE) diagram, sanukitoids display a highly fractionated pattern [$(La/Yb)_N$ varying from 7.83 to 68.94, avg. = 29.8] with a negative Eu anomaly (Eu/Eu* varying from 0.96 to 0.20, avg. = 0.63) (**Figure 6A**). On the primitive mantle normalized multi-elemental variation diagram, the sanukitoids display prominent Large Ion Lithophile Elements (LILE) enrichment and High Field Strength Elements (HFSE) depletion (**Figure 6B**). These rocks exhibit negative anomalies of Nb,Ta, Sr, and Ti.

TABLE 1 | Major and trace elemental compositions of the Kanker granites.

	Biotite and two-mica granites							
Sample	B/5A	B/5B	B/6	BB14-1	S/240/3	S/230/4	S/237/3	S/239/1
SiO_2 (wt. %)	73.11	73.22	72.17	73.31	74.09	73.32	74.07	73.12
Al_2O_3	14.83	14.79	14.91	14.99	14.63	14.77	14.44	14.61
Fe_2O_3 (T)	1.50	1.63	1.74	1.38	1.41	1.47	1.30	1.45
MnO	0.02	0.02	0.03	0.01	0.03	0.02	0.02	0.02
MgO	0.20	0.22	0.22	0.16	0.14	0.12	0.19	0.18
CaO	1.03	1.10	1.07	1.23	0.96	0.81	0.90	1.05
Na_2O	3.96	3.63	3.76	3.89	3.59	3.72	3.83	3.78
K_2O	5.02	5.06	4.96	5.12	4.81	4.92	4.93	5.03
TiO_2	0.08	0.07	0.15	0.05	0.08	0.10	0.13	0.13
P_2O_5	0.03	0.03	0.05	0.01	0.01	0.01	0.02	0.04
LOI	0.44	0.63	0.54	0.35	0.42	0.51	0.35	0.35
Sum	100.22	100.39	99.60	100.50	100.15	99.78	100.18	99.78
Mg#	22.48	22.71	21.96	20.47	17.92	15.69	24.19	21.62
A/CNK	1.07	1.10	1.10	1.06	1.14	1.14	1.09	1.08
A/NK	1.24	1.29	1.29	1.25	1.32	1.29	1.24	1.25
Cr (ppm)	16.03	15.07	14.75	86.15	79.51	80.05	79.62	77.04
Co	1.92	1.89	2.44	1.83	2.14	1.82	2.14	2.52
Ni	2.75	3.94	2.80	6.01	6.42	6.23	5.54	5.58
Rb	296	270	263	287	270	332	207	209
Sr	35.61	59.46	68.89	39	34	34.8	75.9	79
Cs	1.99	1.75	2.42	1.18	1.13	0.679	0.528	0.22
Ba	180	267	242	115	73	89.9	140	201
Sc	1.92	1.49	1.59	2.18	4.22	1.53	1.32	1.26
V	0.56	0.64	1.10	8.42	4.46	4.49	6.09	8.05
Ta	2.85	2.08	3.06	1.62	0.89	1.34	1.01	0.31
Nb	19.9	14.8	20.7	13.23	35.31	31.91	23.81	20.35
Zr	60.91	77.01	123	137	213	274	191	140
Hf	2.85	3.07	4.70	4.57	7.44	10.5	6.37	4.19
Th	31.98	33.59	31.25	21.06	52.48	61.0	44.6	24.67
U	10.45	14.64	19.70	9.53	15.26	12.1	9.56	9.69
Y	28.34	23.49	21.82	16.19	45.15	43.5	24.8	26.11
La	134	210	149	101	106	202	206	120
Ce	101	148	109	69.63	79.38	137	139	87.22
Pr	60.36	91.61	73.07	56.54	74.87	112	108	76.06
Nd	39.45	57.71	49.43	33.47	50.22	65.07	58.90	46.69
Sm	24.03	30.44	28.24	21.35	41.83	40.85	30.02	31.31
Eu	3.69	4.85	5.52	3.23	3.80	4.89	6.38	5.81
Gd	13.36	15.46	14.84	11.10	24.83	21.38	14.98	16.57
Tb	14.80	14.89	13.83	11.94	32.64	24.89	15.51	19.12
Dy	16.22	14.18	13.91	8.69	27.25	20.08	11.66	15.04
Ho	13.60	11.33	10.89	6.67	21.73	16.57	9.17	11.65
Er	14.16	11.05	10.35	7.35	23.57	19.00	10.16	12.29
Tm	14.73	10.78	9.81	8.06	24.61	20.94	10.75	11.86
Yb	17.23	11.96	10.64	8.52	23.05	21.02	10.30	10.61
Lu	19.60	14.06	12.20	9.34	22.99	22.33	10.30	10.07
$\sum$REE	485	647	510	357	556	727	641	475
(La/Yb)cn	8.02	18.15	14.44	12.28	4.74	9.92	20.68	11.73
(La/Sm)cn	5.74	7.12	5.43	4.89	2.61	5.10	7.09	3.97
(Gd/Yb)cn	0.78	1.29	1.39	1.30	1.08	1.02	1.45	1.56
(Eu/Eu*)	0.20	0.21	0.26	0.20	0.11	0.16	0.29	0.24
(Zr/Hf)	21.37	25.12	26.23	29.91	28.63	26.00	30.04	33.54
(Nb/Ta)	6.96	7.11	6.77	8.17	39.75	23.77	23.51	64.93
(Sr/Y)	1.26	2.53	3.16	2.39	0.76	0.80	3.06	3.01

	Sanukitoids											
Sample	B16/2	B16/5	B16/9	B16/13	B16/16	B16/36	B16/38	B16/40	S/236/2	S/236/5	S/227/4	S/239/5
SiO_2 (wt. %)	68.16	67.95	67.16	67.30	66.95	67.42	68.16	68.03	69.05	69.04	69.01	63.88
Al_2O_3	12.73	14.08	14.56	14.33	14.96	14.87	14.18	14.73	14.81	14.80	14.27	15.52
Fe_2O_3 (T)	4.22	3.55	3.80	3.69	4.43	4.24	4.12	3.97	3.66	3.55	3.78	5.50
MnO	0.05	0.04	0.04	0.04	0.03	0.06	0.05	0.04	0.03	0.03	0.05	0.04
MgO	1.71	1.32	1.46	1.47	1.96	1.56	1.32	1.29	1.29	1.25	1.19	3.11
CaO	3.03	2.99	2.87	2.76	3.37	2.87	2.94	2.75	2.72	2.83	2.75	3.53
Na_2O	3.77	3.84	3.86	4.01	3.61	3.25	4.02	3.59	3.13	3.72	2.73	3.31
K_2O	5.35	5.12	5.14	5.00	3.52	5.15	4.27	4.30	4.62	3.40	4.62	4.28
TiO_2	0.55	0.46	0.45	0.58	0.54	0.44	0.37	0.41	0.44	0.42	0.43	0.60
P_2O_5	0.42	0.23	0.26	0.26	0.52	0.13	0.19	0.19	0.17	0.27	0.36	0.23
LOI	0.42	0.35	0.46	0.52	0.39	0.43	0.51	0.58	0.41	0.40	0.54	0.47
Sum	100.42	99.95	100.06	99.97	100.28	100.43	100.11	99.88	100.33	99.71	99.73	100.47
Mg#	47.19	45.04	45.77	46.75	49.35	44.78	41.39	41.72	43.75	43.65	40.84	55.46
A/CNK	0.73	0.81	0.85	0.84	0.94	0.92	0.86	0.95	0.98	0.99	0.98	0.94
A/NK	1.06	1.19	1.22	1.19	1.54	1.36	1.26	1.39	1.46	1.51	1.50	1.54
Cr (ppm)	105	110	112	130	137	103	104	124	63.70	62.22	105	71.47
Co	10.63	3.70	8.16	7.64	12.79	3.76	5.37	4.99	3.21	5.64	8.12	13.27
Ni	9.14	8.42	12.26	11.00	9.07	8.26	7.53	9.30	6.04	5.44	6.75	6.89
Rb	140	243	269	324	107	116	107	104	200	100	149	163
Sr	254	158	186	145	485	251	329	306	241	465	453	450
Cs	0.30	1.04	3.04	1.99	1.03	0.69	0.60	0.88	0.93	0.84	0.31	0.69
Ba	1134	1025	774	809	1068	1399	1036	1257	1418	1235	1852	1388
Sc	8.73	4.79	9.50	7.90	7.37	6.86	8.92	10.27	3.14	4.56	8.97	9.78
V	35.55	16.10	39.07	33.13	62.68	16.94	26.17	24.32	12.34	31.48	42.47	62.1
Ta	0.94	0.76	1.74	0.28	0.80	0.09	0.09	0.07	1.37	0.70	0.84	1.49
Nb	34.04	17.95	30.88	47.48	22.74	7.89	10.38	7.17	20.65	17.57	20.44	18.54
Zr	690	482	463	1137	431	348	482	640	343	333	538	495
Hf	12.80	10.13	8.88	22.15	8.18	6.77	9.26	12.60	7.38	6.63	11.33	10.61
Th	43.89	74.58	53.80	143	3.49	11.71	14.99	14.80	20.19	15.15	23.88	21.38
U	8.03	11.21	11.58	36.65	2.43	1.83	1.65	2.07	8.50	2.73	8.37	3.86
Y	36.00	24.95	64.50	76.66	67.08	21.38	23.08	20.19	20.45	13.97	18.29	34.65
La	341	504	430	1086	138	198	256	224	319	279	381	349
Ce	235	347	289	762	107	131	165	145	202	171	249	241
Pr	207	278	226	614	104	107	134	117	158	132	197	204
Nd	134	161	129	349	74.26	63.57	79.35	70.91	89.25	74.87	114	130
Sm	77.39	81.47	71.47	184	67.77	34.54	41.91	36.68	39.34	32.77	48.33	68.27
Eu	27.28	21.07	20.14	26.78	29.25	21.18	22.85	23.19	19.32	22.75	29.18	36.53
Gd	36.61	35.68	37.76	85.21	46.86	16.37	20.22	18.33	17.32	14.93	20.16	31.94
Tb	35.33	31.67	44.88	81.97	53.95	16.65	19.42	18.27	15.81	12.67	15.64	30.20
Dy	22.87	18.47	34.71	52.91	42.19	11.79	13.88	12.55	11.25	8.48	9.94	21.13
Ho	16.17	11.43	27.89	36.11	30.89	9.00	10.59	9.20	8.77	6.28	7.50	15.61
Er	16.54	9.96	30.53	32.97	28.94	9.91	11.12	9.80	9.71	6.68	8.55	16.56
Tm	15.54	8.33	32.99	28.73	23.44	11.20	11.31	10.03	10.54	6.67	9.65	17.14
Yb	13.98	7.56	32.12	23.92	18.21	11.18	12.06	9.81	10.69	6.74	11.20	17.29
Lu	13.40	7.20	31.73	21.84	16.15	12.20	11.91	10.25	10.92	7.51	14.26	18.45
$\sum$REE	1192	1523	1439	3385	781	654	810	716	922	782	1116	1197
(La/Yb)cn	25.22	68.94	13.83	46.93	7.83	18.34	21.96	23.60	30.84	42.72	35.12	20.87
(La/Sm)cn	4.55	6.39	6.21	6.09	2.10	5.93	6.31	6.31	8.37	8.78	8.13	5.28
(Gd/Yb)cn	2.62	4.72	1.17	3.56	2.57	1.46	1.68	1.87	1.62	2.21	1.80	1.85
(Eu/Eu*)	0.48	0.36	0.37	0.20	0.51	0.84	0.74	0.85	0.69	0.96	0.86	0.73
(Zr/Hf)	53.87	47.59	52.07	51.31	52.63	51.37	52.06	50.80	46.43	50.19	47.53	46.61
(Nb/Ta)	36.19	23.57	17.75	171	28.45	86.07	116	106	15.04	24.98	24.23	12.44
(Sr/Y)	7.04	6.34	2.88	1.90	7.24	11.75	14.26	15.13	11.78	33.26	24.78	12.99

	Hybrid granites																		
Sample	B16/1	B16/17	B16/22	B16/25	B16/29	B16/31	B16/33	B16/35	B/258/3	B/259/1	B/259/2	B/8A	B/8B	B/10	B/11	B/27	BB14-3	S/230/10	S/147/2
SiO_2 (wt. %)	71.90	71.29	70.27	69.31	71.45	71.21	69.94	71.49	70.27	71.50	71.93	70.70	69.83	71.01	69.93	69.81	71.30	71.29	73.38
Al_2O_3	14.28	14.87	15.76	14.69	14.62	14.91	14.41	14.56	14.60	14.48	13.85	14.96	15.02	14.81	14.87	15.10	14.57	13.77	13.80
Fe_2O_3 (T)	1.90	2.30	1.95	3.28	2.46	2.19	2.56	2.69	2.93	2.87	2.57	2.84	2.69	1.92	2.45	2.54	2.37	3.30	2.33
MnO	0.01	0.01	0.02	0.03	0.02	0.02	0.02	0.02	0.03	0.02	0.02	0.02	0.02	0.03	0.03	0.03	0.02	0.03	0.02
MgO	0.42	0.34	0.89	0.94	0.36	0.49	0.54	0.34	0.69	0.84	0.64	0.36	0.60	0.42	0.36	0.62	0.74	0.55	0.34
CaO	1.74	1.48	2.25	2.61	1.87	1.90	2.48	2.04	1.20	1.47	1.41	2.15	1.82	2.59	1.43	2.77	2.03	1.65	1.69
Na_2O	3.09	3.38	5.00	2.95	3.54	3.88	3.36	3.84	4.14	3.94	3.32	3.32	3.49	3.47	3.20	4.35	4.39	3.96	3.19
K_2O	5.38	4.97	2.79	4.91	4.46	4.15	5.29	4.52	4.36	4.12	4.20	4.90	4.58	4.81	5.59	3.97	3.43	3.90	4.97
TiO_2	0.17	0.25	0.28	0.40	0.23	0.22	0.25	0.23	0.27	0.32	0.24	0.26	0.31	0.17	0.19	0.28	0.27	0.43	0.10
P_2O_5	0.06	0.07	0.05	0.22	0.09	0.11	0.08	0.09	0.08	0.05	0.05	0.16	0.12	0.12	0.08	0.11	0.13	0.09	0.03
LOI	0.42	0.49	0.31	0.46	0.43	0.55	0.58	0.32	0.70	0.59	0.73	0.61	0.63	0.71	0.64	0.58	0.42	0.51	0.42
Sum	99.37	99.45	99.56	99.81	99.51	99.62	99.50	100.15	99.28	100.20	98.97	100.27	99.10	100.04	98.76	100.15	99.67	99.48	100.27
Mg#	32.59	24.65	50.18	38.76	24.41	32.87	31.54	22.00	34.02	39.03	35.22	21.74	32.76	32.31	24.20	34.97	40.78	26.65	24.44
A/CNK	1.02	1.09	1.03	0.99	1.04	1.04	0.91	0.97	1.06	1.06	1.10	1.02	1.07	0.95	1.07	0.92	1.00	1.00	1.01
A/NK	1.31	1.36	1.40	1.44	1.37	1.37	1.28	1.30	1.26	1.32	1.38	1.39	1.40	1.36	1.31	1.32	1.33	1.28	1.30
Cr (ppm)	125.32	105	113	108	96.25	110	144	103	13.73	13.25	14.57	11.83	11.58	13.45	15.35	9.99	83.78	83.44	82.14
Co	3.94	3.00	4.40	6.05	3.60	3.89	4.46	3.87	2.90	2.26	3.28	3.17	3.74	2.68	2.89	4.09	4.95	3.69	2.45
Ni	8.95	7.95	10.06	8.85	9.58	7.50	12.88	8.74	3.25	2.87	3.29	3.12	3.44	3.22	7.70	3.47	6.68	6.21	6.14
Rb	230	143	123	206	101	91	221	152	99	97	113	176	169	181	200	117	65	210	125
Sr	121	111	204	172	243	286	133	172	51	32	28	147	201	206	109	356	236	105	149
Cs	0.41	0.56	4.02	0.92	0.78	1.04	2.94	0.69	1.63	0.95	1.10	2.59	1.68	2.05	3.49	2.05	0.53	1.19	0.90
Ba	712	459	464	827	1295	983	445	958	1118	983	1025	800	836	925	664	695	875	498	952
Sc	6.03	5.16	6.71	6.26	5.75	6.70	10.49	7.82	3.73	3.42	3.55	2.71	2.68	2.59	2.17	3.07	3.63	3.77	2.20
V	11.60	11.26	31.92	35.07	14.16	14.49	19.05	15.05	1.09	0.91	0.79	1.29	1.54	0.89	0.94	1.94	14.84	11.83	8.67
Ta	2.11	0.57	0.84	0.41	0.34	0.32	0.11	0.07	1.60	2.10	2.54	1.11	0.67	2.17	1.73	0.91	0.29	1.21	0.28
Nb	32.42	11.31	14.99	24.03	10.74	7.44	10.55	9.25	26.59	29.16	33.77	16.34	12.81	20.28	16.16	8.67	11.81	27.15	4.08
Zr	382	304	571	461	443	239	343	364	207	212	293	218	260	167	171	135	406	578	219
Hf	8.59	6.63	11.66	9.20	8.60	5.02	7.67	7.67	6.95	7.35	9.89	6.63	7.67	5.92	6.05	4.02	8.30	13.53	5.79
Th	59.32	45.81	50.28	48.79	12.56	11.64	54.23	25.21	12.02	26.04	22.26	27.27	34.45	39.20	38.63	14.54	25.90	76.95	10.72
U	12.17	6.03	4.80	10.92	1.98	1.41	13.12	3.91	2.58	5.51	7.13	5.62	3.91	12.57	9.55	4.74	1.39	28.42	2.59
Y	27.95	9.06	19.67	31.25	13.52	7.11	23.06	17.08	42.55	51.76	66.46	19.50	10.31	21.18	12.83	8.52	11.50	40.91	6.68
La	335	482	381	384	189	159	307	271	211	254	382	300	382	265	256	125	309	1123	84.91
Ce	236	334	252	250	123	116	200	181	172	182	314	206	292	179	178	84.57	202	703	60.81
Pr	189	256	197	193	99.65	84.39	157	146	109	129	189	129	157	113	114	54.16	159	555	52.90
Nd	109	137	110	110	58.97	50.86	89.91	85.17	82.66	95.71	138	83.50	99.05	75.60	75.49	37.14	90.51	289.33	33.01
Sm	59.10	57.25	56.88	56.14	30.35	23.51	46.86	41.87	48.25	56.42	77.29	36.02	38.88	39.90	38.36	18.56	42.97	116.64	17.58
Eu	14.27	11.97	15.28	27.33	22.13	14.62	17.37	21.93	15.31	13.92	16.69	10.41	11.21	7.93	8.76	9.01	19.12	12.12	13.18
Gd	28.65	20.93	25.79	28.50	13.93	9.70	21.79	18.05	28.47	32.45	45.03	16.98	16.29	20.39	17.91	8.70	18.85	47.33	7.18
Tb	27.77	13.24	22.29	26.71	12.19	7.87	20.85	16.15	28.55	31.80	42.32	13.74	10.17	17.96	13.13	6.89	15.45	38.74	6.20
Dy	19.00	6.68	13.68	18.30	7.94	4.60	14.42	10.46	28.99	32.16	42.58	12.53	7.78	15.48	10.11	5.88	9.03	24.61	4.02
Ho	13.42	4.24	9.04	14.04	6.10	3.23	10.69	7.75	22.72	25.53	34.10	9.75	5.88	11.13	7.34	4.53	5.76	17.44	2.90
Er	12.39	4.04	8.50	15.34	6.33	3.26	11.04	7.84	20.88	24.27	33.34	8.84	5.38	9.65	6.51	4.25	5.03	18.53	3.10
Tm	11.75	3.84	7.78	16.11	6.47	3.41	11.43	8.68	19.05	23.02	32.57	7.93	4.88	8.17	5.68	3.97	4.14	19.13	3.38
Yb	11.26	3.82	7.46	16.60	6.34	3.25	11.11	8.69	19.90	24.94	36.41	8.08	5.08	7.96	5.75	4.12	3.64	19.45	3.69
Lu	12.33	3.89	8.51	17.01	7.83	3.47	11.98	10.03	22.19	28.39	42.05	9.28	6.03	8.91	7.00	5.39	3.88	20.69	4.46
$\sum$REE	1080	1339	1115	1174	590	487	932	835	829	954	1426	851	1041	781	744	372	888	3005	297
(La/Yb)cn	30.75	130	52.82	23.94	30.84	50.64	28.52	32.20	10.94	10.52	10.84	38.33	77.71	34.44	46.02	31.34	87.65	59.70	23.78
(La/Sm)cn	5.85	8.70	6.92	7.07	6.44	7.00	6.76	6.68	4.51	4.65	5.10	8.59	10.13	6.87	6.89	6.95	7.43	9.94	4.99
(Gd/Yb)cn	2.54	5.47	3.46	1.72	2.19	2.98	1.96	2.08	1.43	1.30	1.24	2.10	3.21	2.56	3.11	2.11	5.17	2.43	1.94
(Eu/Eu*)	0.33	0.31	0.37	0.65	1.01	0.89	0.51	0.74	0.40	0.32	0.27	0.40	0.41	0.26	0.31	0.66	0.62	0.15	1.07
(Zr/Hf)	44.47	45.82	48.92	50.10	51.50	47.74	44.74	47.50	29.70	28.85	29.65	32.95	33.93	28.27	28.28	33.52	48.95	42.70	37.78
(Nb/Ta)	15.40	19.72	17.81	59.30	31.77	23.23	94.02	142	16.58	13.87	13.29	14.71	19.11	9.35	9.37	9.51	41.12	22.35	14.74
(Sr/Y)	4.32	12.23	10.36	5.51	17.97	40.21	5.76	10.09	1.21	0.62	0.43	7.52	19.50	9.75	8.50	41.75	20.56	2.57	22.32

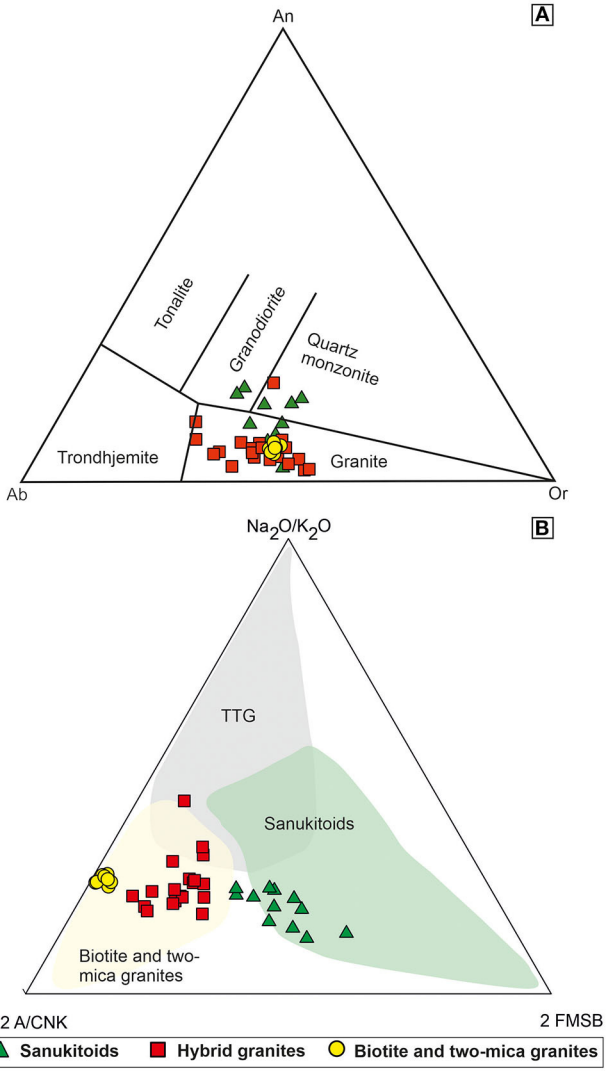

FIGURE 4 | (A) The distribution of Kanker granites on the normative An-Or-Ab triangle diagram (after O'Connor, 1965). **(B)** The disposition of the Kanker granites in the ternary classification diagram for Neoarchean granitoids (after Laurent et al., 2014), the fields correspond to that of well-studied suits from different cratons.

Biotite and Two-Mica Granites

Based on the normative mineralogy, the biotite and two-mica granites are essentially granites (**Figure 4A**). Their silica and alumina compositions vary in a narrow range, between 72 and 74 wt.% and 14–15 wt.%, respectively (**Table 1**). These granites are essentially potassic (K_2O = 4.9–5.1 wt.%) with peraluminous affinity (A/CNK >1) and belongs to high-K calc-alkaline series (**Figures 5A,B**). These rocks have lower compositions of ferromagnesian elements (Fe_2O_3+MnO+MgO+TiO_2 <2.2 wt.%) and are clustered toward the Alumina pole in the classification diagram for Archean granitoids (**Figure 4B** and **Table 1**). They have a low Mg number (Mg# <22) (**Figure 5C**). In Harker variation diagrams, these granites show negative correlation of CaO, MgO, TiO_2, and Fe_2O_3 (**Figure 5**). The biotite and two-mica granites have low transition elemental compositions (**Table 1**), have high Rb (avg. Rb = 267 ppm) and low Sr (avg. Sr = 53 ppm), resulting in high Rb/Sr ratios (avg. Rb/Sr = 5.9). Similarly, these granites have low Zr (avg. Zr = 152 ppm) and Hf (avg. Hf = 5.4 ppm), resulting in low Zr/Hf ratios (avg. Zr/Hf = 27.6).

On the chondrite normalized REE plot, the biotite and two-mica granites are less fractionated with $(La/Yb)_N$ varying from 4.74 to 20.68 (avg. $(La/Yb)_N$ = 12.5), but possess a strong negative Eu anomaly with Eu/Eu^* <0.3 (**Figure 6C**). On the multi-elemental variation diagram, biotite and two-mica granites display LILE enrichment and HFSE depletion with negative anomalies of Ba, Nb, Ta, Eu, Sr, and Ti (**Figure 6D**). The Nb-Ta depletion is not very prominent in the biotite and two-mica granites when compared to the sanukitoids.

Hybrid Granites

The hybrid granites of the Bastar Craton are compositionally diverse, with geochemical features intermediate between the sanukitoids and the biotite and two-mica granites. Based on normative mineralogy, they are granites (**Figure 4A**). Their silica and alumina compositions range between 69 and 73 and 13–16 wt.%, respectively (**Table 1**). On the Alumina Saturation Index diagram (Shand, 1943), the hybrid granites are distributed between metaluminous and peraluminous fields, with more affinity toward the latter (**Figure 5A**). These are potassic (K_2O = 2.8–5.6 wt.%), plotting in the fields of high-K calc-alkaline to shoshonitic series (**Figure 5B**). They have varied Mg number, ranging between 21 and 55 (avg. Mg# = 32) (**Figure 5C**). On Harker variation diagrams, the compositions of hybrid granites are distributed between the sanukitoids and biotite and two-mica granites (**Figures 5D–F**). These granites are low in ferromagnesian elements (1.8 ≤ FMMT ≤ 4.5 wt.%) (**Table 1**).

On the chondrite normalized REE plot, hybrid granites show incoherent REE abundances with a strongly fractionated elemental pattern [$(La/Yb)_N$ range from 10.5 to 130, avg. = 42] and variably negative Europium anomalies (between 0.15 and 1) (**Figure 6E**). On the primitive mantle normalized multi-elemental variation diagram, hybrid granites display LILE enrichment and HFSE depletion, with the trend intermediate between sanukitoids and biotite and two-mica granites (**Figure 6F**).

PETROGENESIS OF THE KANKER GRANITES

Source

Sanukitoids are considered to be derived from an incompatible element rich mantle source (Shirey and Hanson, 1984). Sanukitoids of the Kanker area are metaluminous, low in SiO_2, and high in ferromagnesian elements (**Figures 4B**, **5A**). They are also rich in transition metals and incompatible elements such as Ba and Sr (avg. Ba+Sr = 1510 ppm) (**Table 1**). Such compositional diversity (rich in compatible and incompatible elements) is suggestive of an enriched mantle source (**Figure 7**) (Shirey and Hanson, 1984; Heilimo et al., 2010). It has been

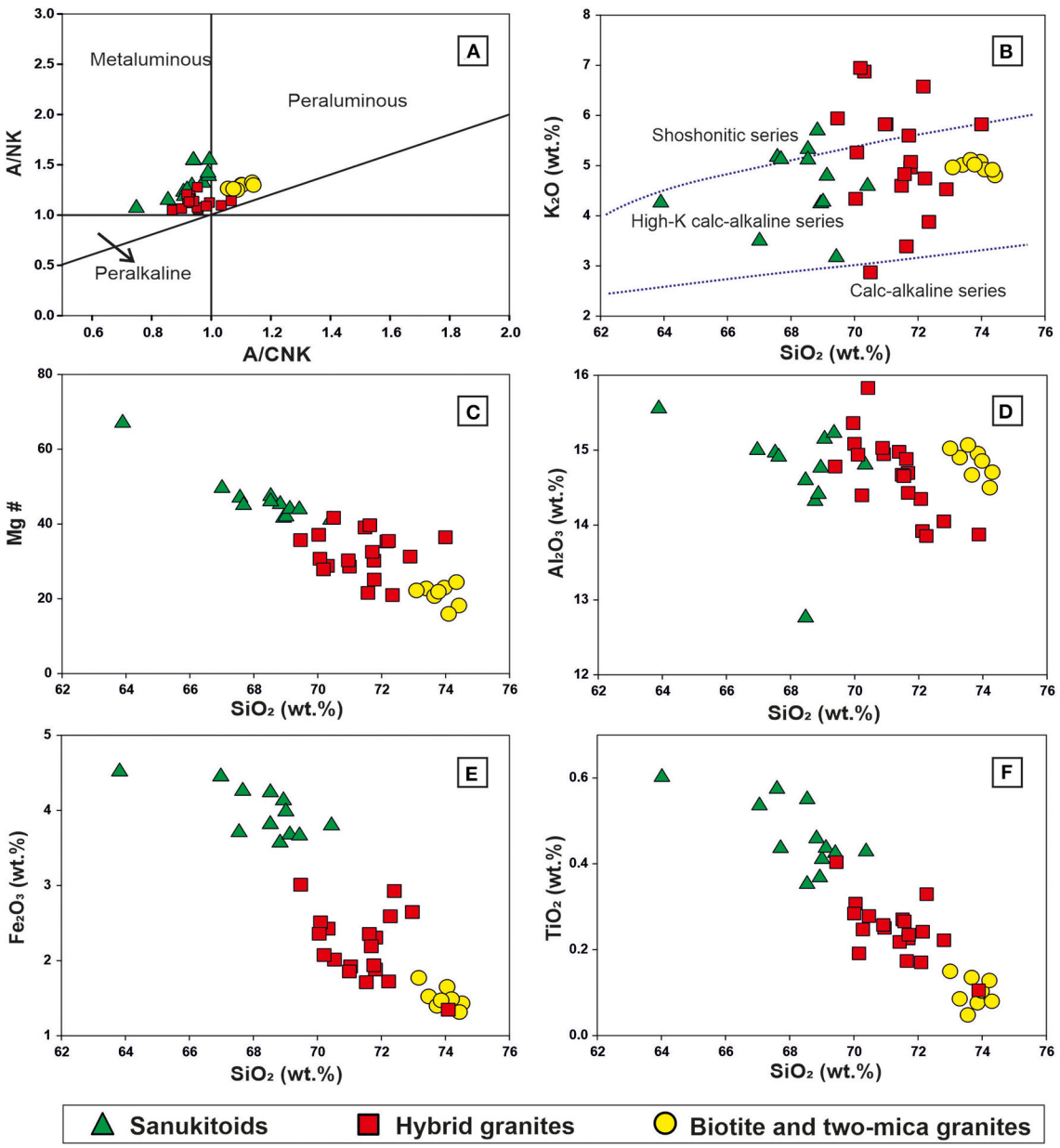

FIGURE 5 | (A) Alumina Saturation Index diagram (Shand, 1943), wherein the sanukitoids are confined to metaluminous field, biotite and two-mica granites are into peraluminous field. The hybrid granites are distributed among both fields. **(B)** SiO_2 vs. K_2O diagram (after Le Maitre, 1989) to show the variations in the melt affinity of different granite types of Kanker pluton. **(C)** SiO_2 vs. Mg# plot, wherein the sanukitoids with high Mg# suggest the mantle involvement (Rapp et al., 1999). **(D–F)** Harker variation diagrams depicting the major elemental compositional variations among the granite types of Kanker pluton. Note the compositional variability of hybrid granites and their distribution between the compositional range of sanukitoids and biotite and two-mica granites.

established that enrichment of the mantle can be caused by different metasomatic agents such as slab melts, carbonatite veins, fluids and/ or sediment melts (Smithies and Champion, 2000; Halla, 2005; Steenfelt et al., 2005; Martin et al., 2009; Laurent et al., 2011). In the slab melt model, petrogenesis of sanukitoids is explained by a two-stage process involving the interaction between slab melts and the mantle peridotite (Martin et al., 2009; Laurent et al., 2014). The sanukitoids from the Kanker are relatively poor in Sr (avg. Sr =310 ppm) when compared to the other well-studied sanukitoids, such as those from the Dharwar Craton (avg. Sr = 664 ppm; Mohan et al., 2019), Kapvaal Craton (avg. Sr = 553 ppm; Laurent et al., 2014) and Karelian and Kola cratons (avg. Sr = 729 ppm; Halla et al., 2009). The low Sr concentration could also be induced by plagioclase fractionation. The rocks have low Sr/Y values (Sr/Y $\leq$40), which rules out the role of slab melting in the metasomatisation of the mantle

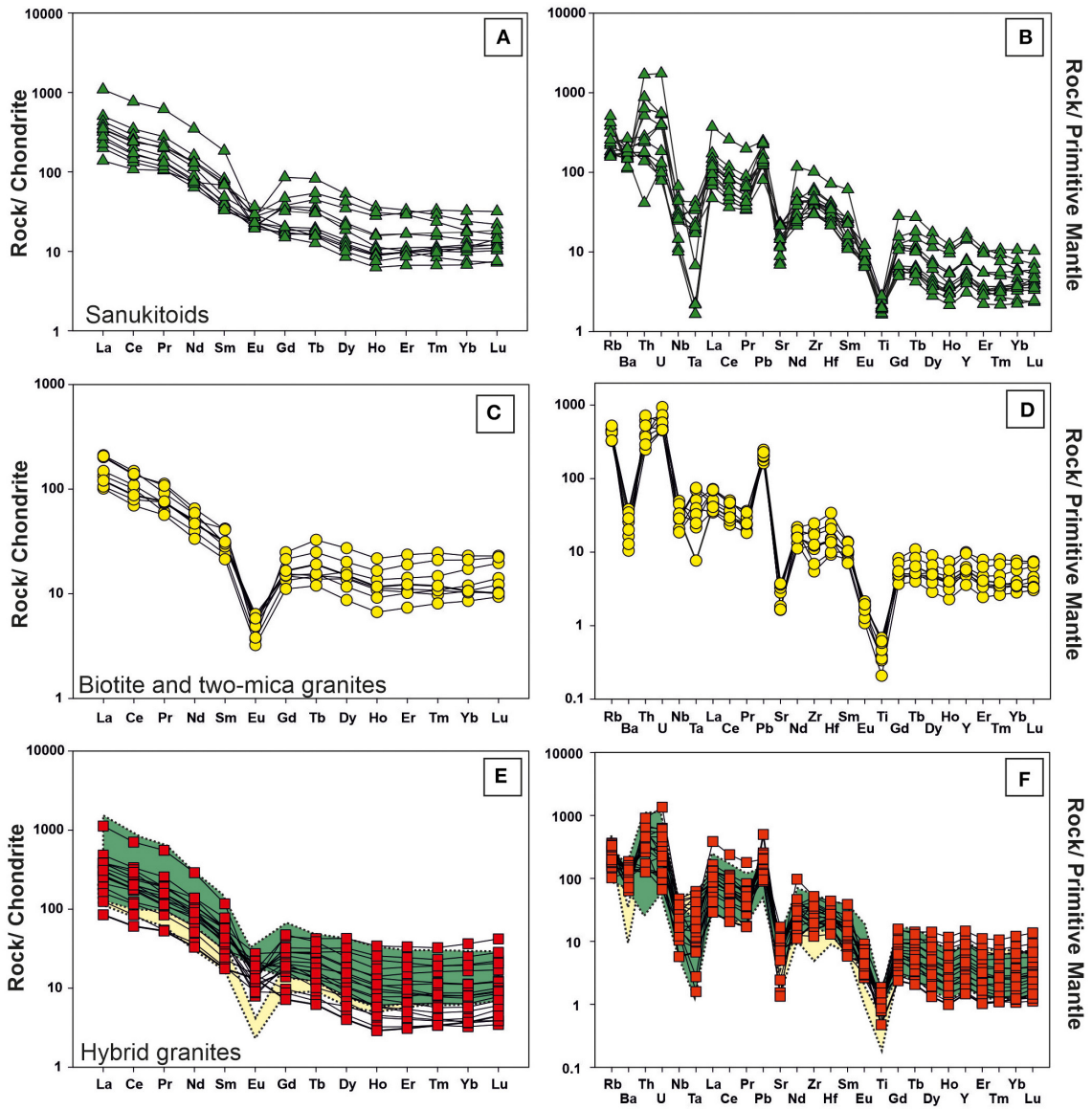

FIGURE 6 | Chondrite-normalized Rare earth element (REE) and primitive mantle-normalized multi-elemental variation diagram for the sanukitoids **(A,B)**, biotite and two-mica granites **(C,D)** and hybrid granites **(E,F)**. The compositional range of sanukitoids (green area) and biotite and two-mica granites (yellow area) are highlighted in the background **(E,F)** to show that hybrid granites are the mixtures of two primary granite types. Normalized values are from Sun and McDonough (1989).

(Martin et al., 2009). Also, Neoarchean TTG magmatism is yet to be reported from this craton. The lower Sr and Ca compositions, and corresponding enrichment of the HFSE (such as Nb, up to 47 ppm and Zr, up to 1,137 ppm) rules out the possibility of carbonate melt as a metasomatic agent in the genesis of these sanukitoids (Steenfelt et al., 2005). Also, there is no record of carbonatite magmatism in the vicinity of the study area.

Mantle enrichment can also be possible due to the involvement of subducting fluids (Elliott, 2004) and/ or due to sediment melting associated with the subducting oceanic crust (Woodhead et al., 2001). Trace elemental ratios such as Ba/La, U/Th, Th/Yb, Hf/Sm, and Ta/La can effectively differentiate between the fluid-related and sediment-melt related enrichments (Hawkesworth et al., 1997; La Flèche et al., 1998; Woodhead et al., 2001). The Bastar sanukitoids and a few hybrid granites follow the trend of sediment-melt related enrichment (**Figure 8A**). The above observation is also supported by the disposition of these samples in the Hf/Sm vs. Ta/La plot (**Figure 8B**). The available detrital zircon age data from the Bastar Craton indicates very older provenance, as old as extending from the Paleoproterozoic to Paleoarchean (1.75–3.67 Ga) (Khanna et al., 2019). Thus, the mantle enrichment, as evident in the case of Kanker sanukitoids, is possibly an outcome of sediment melting associated with earlier episode(s) of subduction.

The biotite and two-mica granites are considered to be the products of crustal reworking of older TTG with

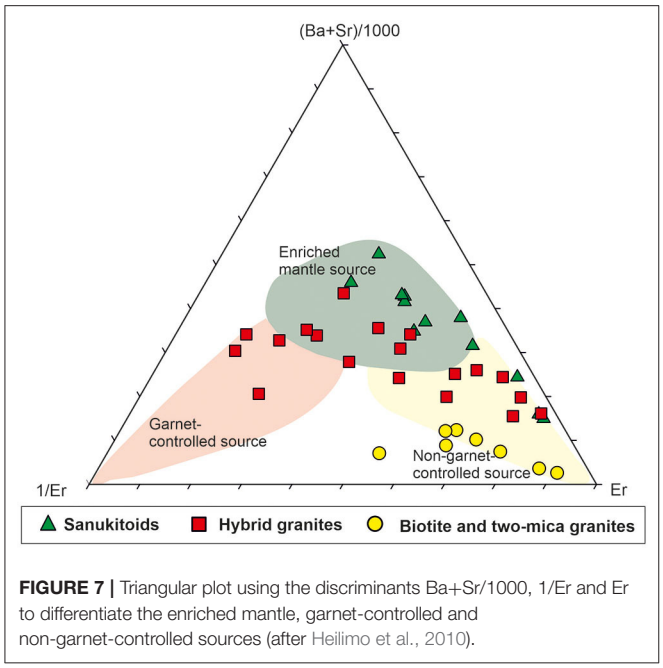

FIGURE 7 | Triangular plot using the discriminants Ba+Sr/1000, 1/Er and Er to differentiate the enriched mantle, garnet-controlled and non-garnet-controlled sources (after Heilimo et al., 2010).

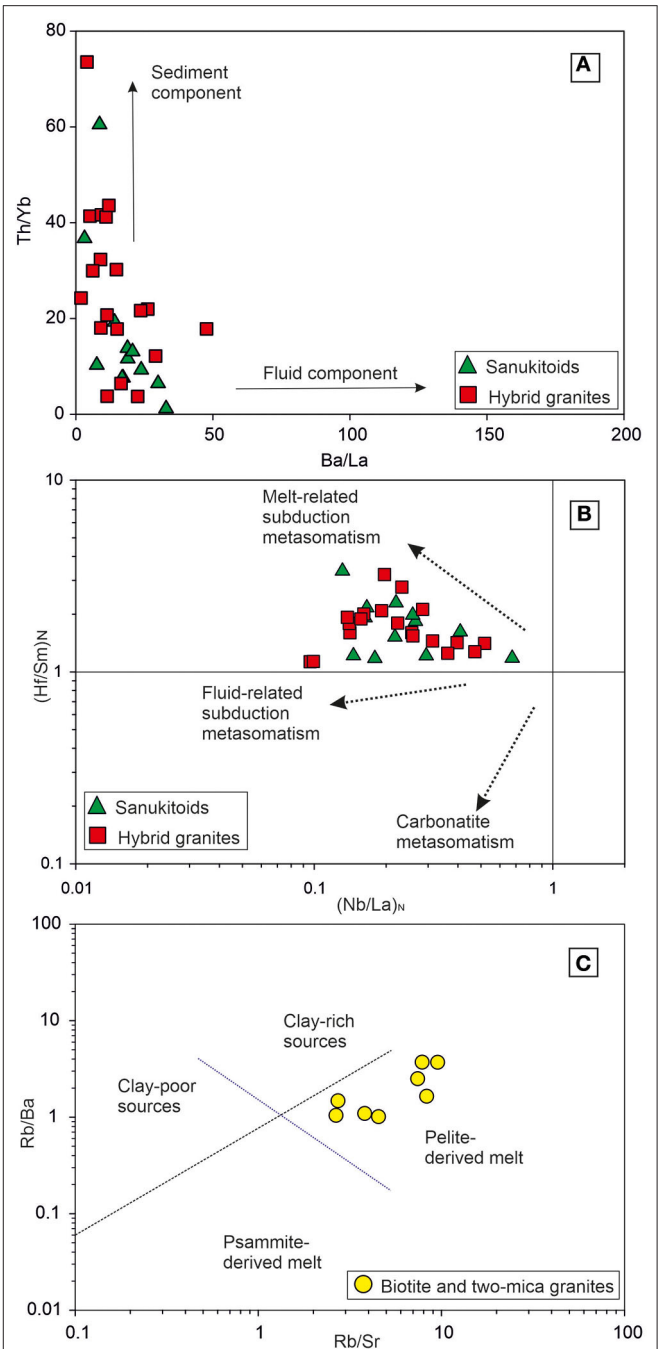

FIGURE 8 | (A) Th/Yb vs. Ba/La plot (Woodhead et al., 2001), to identify the role of sediment and fluid component. **(B)** $(Hf/Sm)_N$ vs. $(Nb/La)_N$ plot (La Flèche et al., 1998), to differentiate the metasomatic agent involved in the petrogenesis of Kanker granites **(C)** Rb/Ba vs. Rb/Sr plot (after Sylvester, 1998), to determine the nature of crustal sediments involved in the petrogenesis of strongly peraluminous biotite and two-mica granites.

sedimentary inputs (Laurent et al., 2014). These granites are SiO_2 rich, peraluminous, and poor in ferromagnesian elements. Paleoarchean basement rocks (TTG) are documented from the Bastar Craton (Sarkar et al., 1993; Ghosh, 2004; Rajesh et al., 2009). Possibly, the reworking of these older basement granitoids (TTG) is responsible for the origin of biotite and two-mica granites of Kanker. Besides, the role of sedimentary inputs in their genesis has been examined. The higher Rb, low Sr and Ba compositions of these strongly peraluminous rocks, and corresponding higher Rb/Ba and Rb/Sr ratios (**Figure 8C**) indicate their genesis from clay-rich sources (Sylvester, 1998). These elements are actively controlled by minerals of the feldspar and mica group (Harris and Inger, 1992). On the ternary source discrimination diagram (**Figure 7**), they are confined to non-garnet- controlled sources. This is further supported by strong negative europium anomaly, low Sr content (avg. 53 ppm) and flat HREE pattern (**Figure 6C**), to suggest the shallow depth of melting where plagioclase was in the source residue. Therefore, the biotite and two-mica granites could have been generated by the crustal melting with significant sediment input, or due to the reworking of older TTG. The availability of radiogenic isotopic data can resolve this preposition.

The hybrid granites are found in different Neoarchean cratons and are formed by variable interaction between the melts of TTG, biotite and two-mica granites and sanukitoids (Laurent et al., 2014; Mohan et al., 2019). The hybrid granites of Kanker possess geochemical compositions intermediate between the sanukitoids and biotite and two-mica granites. This observation is supported by geochemical signatures such as metaluminous to peraluminous affinity (**Figure 5A**), major elemental trends on Harker diagrams (**Figures 5C–F**) and incoherent REE patterns (**Figure 6E**). The large variability in incompatible elemental compositions such as Ba (445–1295 ppm, avg. Ba = 817 ppm), Rb (65–230 ppm, avg. Rb = 148 ppm), Sr (28–230 ppm, avg. Sr = 161 ppm) and REE (ΣREE varies from 83 ppm to 910

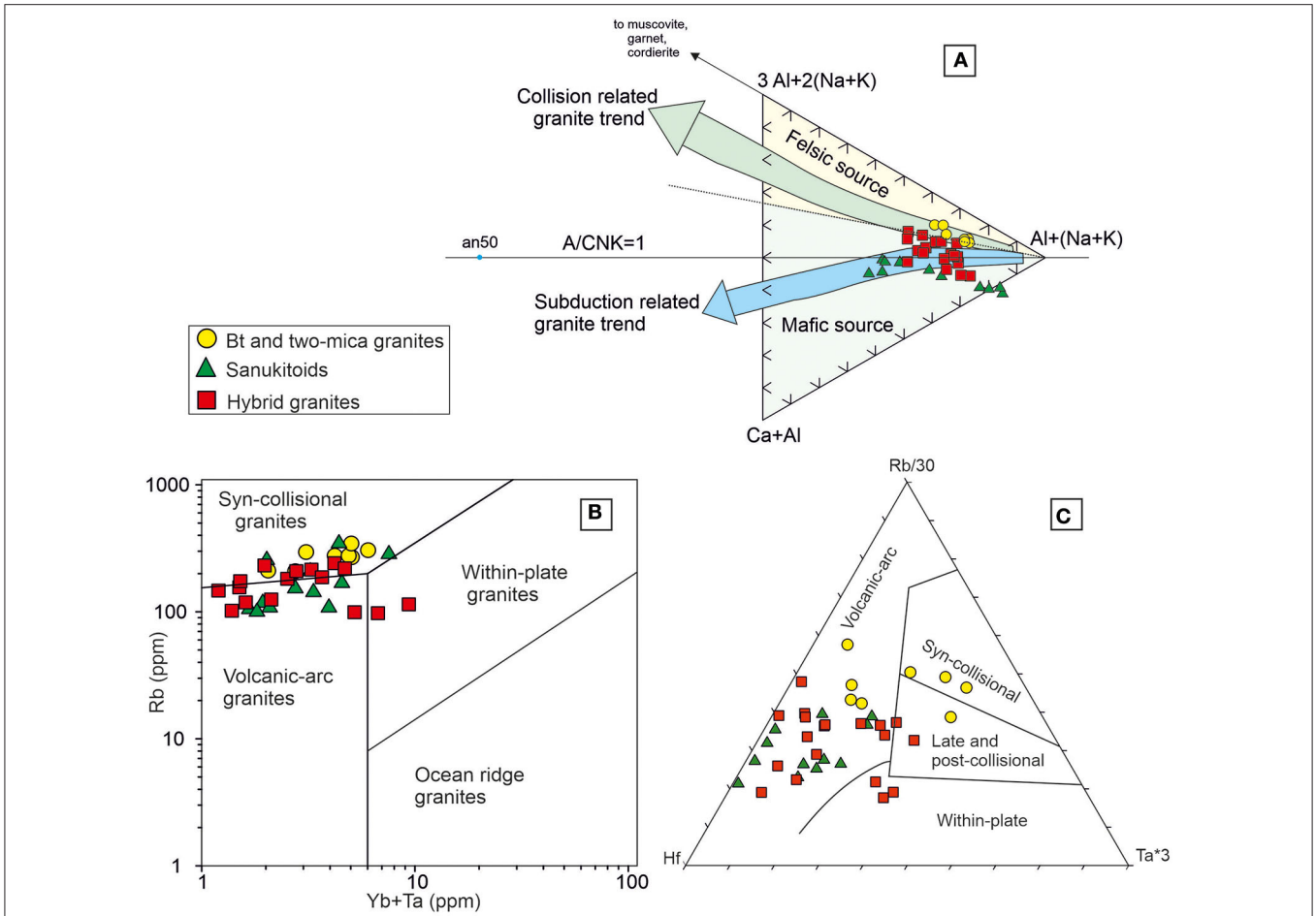

FIGURE 9 | (A) The Ca+Al - 3Al+2(Na+K) - Al+(Na+K) projection diagram to differentiate the sources and the tectonic setting trends in the evolution of granites (Moyen et al., 2017; Moyen and Laurent, 2018). The projection has been plotted using the GCDkit (Janoušek et al., 2016). **(B,C)** are tectonic discrimination diagrams for granites (Pearce et al., 1984; Harris et al., 1986) suggestive of an arc to collisional origin for the Kanker granites.

ppm, avg. ΣREE = 292 ppm), also reflect such heterogeneity. The large range of HFSEs in the hybrid granites could either reflect differentiation, melting depths and/or variable degree of interaction between the magma types. The presence of negative europium anomaly indicates shallow depth of melting or plagioclase fractionation. The geochemical anomalies displayed by these granites are similar to those granitoids that evolved in convergent margins (Pearce et al., 1984). Therefore, the hybrid granites of Kanker possibly had evolved from the melting of a heterogeneous source, formed by variable mixing of crustal and enriched mantle components.

Tectonic Setting

As outlined above, the Kanker granites with large compositional variability are derived from two mutually exclusive end-member sources, i.e., the enriched mantle and an older (felsic) crust. Diversity of these granites and their voluminous distribution within a restricted period during the Archean-Proterozoic transition can only be possible in a tectonic environment where these two distinct source reservoirs were spatially close, and could variably interact due to a heat source. Previous works on the Kanker granites are minimal and ascribe a tectonic setting variable between the subduction and syn-collision (Hussain et al., 2004; Mondal et al., 2006). Based on a compilation of experimental granitic melts, Moyen et al. (2017) devised Ca+Al - 3Al+2(Na+K) - Al+(Na+K) projection diagram to differentiate the mafic and felsic sources responsible for a variety of granitic rocks in arc and collisional systems during the Paleozoic, and further extended it to Archean granitoids (Moyen and Laurent, 2018). In the Ca+Al - 3Al+2(Na+K) - Al+(Na+K) projection diagram (**Figure 9A**), the sanukitoids from the Kanker are confined to the field of mafic source, and fall in the trend of subduction-related tectonic setting. In contrast, the biotite and two-mica granites of the Kanker are confined to the felsic source and fall in the trend of collision-related tectonic setting. The hybrid granites are distributed between the above two groups, indicating their heterogeneous nature, either in source or tectonic setting. Based on the above trend, it may be postulated that the Kanker granites were emplaced in a transitional tectonic setting, involving subduction and collision.

This inference is further supported by the distribution of these samples into the volcanic-arc and syn-collisional granite fields (**Figure 9B**) in the tectonic discrimination diagram (Pearce et al., 1984). A similar distribution is noted for the Kanker granites in the tectonic discrimination diagram of Harris et al. (1986) (**Figure 9C**). Neoarchean granites from many cratons exhibit such a transitional tectonic regime, involving subduction to collision (Laurent et al., 2014; Mohan et al., 2019). Such a transition in tectonic regime is attributed to the changes in geodynamo, and the nature and style of plate tectonics during the Archean-Proterozoic transition (Keller and Schoene, 2012).

In a subduction-collision regime, the subduction episode, prior to the collision results in the metasomatisation of the mantle. In most Archean cratons, sanukitoids represent the terminal event of subduction (Halla et al., 2009; Laurent et al., 2014). The arc magmas often show a transition from fluid fluxed melting to sediment melting with the maturation of subduction (Duggen et al., 2007). As outlined in the earlier section, the Kanker sanukitoids had been derived from the enriched mantle, possibly after the maturation of the arc or after the cessation of subduction. The mantle melts probably underwent differentiation and/or assimilation with the pre-existing older crustal rocks. The heat supplied by these melts resulted in low degree melting of crust with significant sedimentary input to form the peraluminous biotite and two-mica granites. Subsequent to the cessation of subduction, collision between the continental blocks leads to slab break-off, resulting in asthenospheric upwelling (Sylvester, 1998; Bonin, 2004; Halla et al., 2009). Thermal anomaly generated during the collision will induce partial melting of the previously enriched mantle, leading to the interaction between crust and mantle components resulting in the formation of a spectrum of granites (Bonin, 2004; Mikkola et al., 2011; Laurent et al., 2014; Moyen et al., 2017). The compositional heterogeneity of the hybrid granites suggests they could have formed at various stages, i.e., from subduction to collision, or could have resulted by the interaction between enriched mafic magmas with the pre-existing felsic crust. However, precise age and isotopic data will provide better clues on the sequence of emplacement of these granites, constraining the sources and extent of interactions between them. Based on field, geochemical evidences and with the aid of tectonic discrimination diagrams, the evolution of the Kanker granites can be best explained in an accretionary orogenic setting involving the subduction and subsequent collision.

IMPLICATIONS ON REGIONAL GEODYNAMICS

The Bastar Craton remains one of the prominent cratons in the Indian shield, mainly due to the mineralization, proximity to the CITZ and imprints of supercontinental cycles (Pandit and Panigrahi, 2012; Santosh et al., 2018; Liao et al., 2019). In addition to the Kanker, Dongargarh and Malanjkhand are the two other major Archean-Proterozoic granitic plutons. The available geochronological data indicate that these three plutons had emplaced at $\sim$ 2.48 Ga (Sarkar et al., 1993; Panigrahi et al., 2004; Bickford et al., 2014). Having established the subduction to collisional environment responsible for the evolution of the Kanker granites, it is essential to look for the coherence of the proposed tectonic environment with the existing tectonic models proposed for the Dongargarh and Malanjkhand granites.

Available geochemical studies indicate that Malanjkhand granites display I-type affinity (Pandit and Panigrahi, 2012). Also, it has been established that porphyry-type mineralization hosted by this granite was contemporaneous with its emplacement (Stein et al., 2004). The Malanjkhand granites are distributed into the fields of volcanic arc and syn-collisional granites in the tectonic discrimination diagram of Pearce et al. (1984) (refer to Figure 5 of Pandit and Panigrahi, 2012), Although porphyry copper deposits are generally related to convergent margin setting (Sillitoe, 2010), there are also evidences for their occurrences in the collisional environment such as Tibetan Orogen (Hou and Cook, 2009). In the collisional environment, the thermal anomaly associated with the collision could be the source for hydrothermal fluids responsible for the mineralization, as observed in the Malanjkhand granites.

The Dongargarh granite is a complex pluton, with both I- and A-type affinity (Narayana et al., 2000). Previous studies have attributed a continental rift setting for the evolution of the Dongargarh granite (Pandit and Panigrahi, 2012; Manikyamba et al., 2016). The available geochemical data on the intraplate Dongargarh granite, indicate that they are A_2 type granites. The A_2 type granites are considered to be post-orogenic, and are the product of crustal reworking (Eby, 1992; Bonin, 2007). The evolved hafnium isotopic signatures of the Dongargarh granite indicate the reworking of an older crust (Manikyamba et al., 2016). But the A_2 affinity of the Dongargarh granite negates the earlier postulated extensional back-arc or the continental rift environment (Pandit and Panigrahi, 2012; Manikyamba et al., 2016). Therefore, the Dongargarh granite can be related to the collapse of this collisional orogeny due to delamination and thermal relaxation.

To have a better understanding of the prevailing tectonic environment during the emplacement of the Kanker granites, it is imperative to know if any genetic relationship exists between the granites and adjacent supracrustal rocks. An island arc setting is proposed for the siliceous high Mg basalts (SHMB) from the 2.7 Ga Sonakhan Greenstone Belt (SGB), located on the eastern margin of the Kanker granite (Manu Prasanth et al., 2019). The field relationships indicate the intrusive nature of Kanker granites with the Sonakhan belt, suggesting that both lithologies are not contemporaneous (Manu Prasanth et al., 2018). Trace element signatures depict a depleted mantle source for the SGB basalts (Manu Prasanth et al., 2019), distinct from that of the Kanker granites. Geochemical and isotopic studies on the 2.5 Ga volcanic rocks of the Kotri Dongargarh Mobile Belt (KDMB) suggest that they were derived from a depleted mantle source and had evolved in an Andean type continental arc setting (Asthana et al., 2016; Khanna et al., 2019). Hence, it can be surmised that the supracrustals adjacent to the Kanker granites had a different source, and a convergent margin was active in the Bastar Craton during the Neoarchean and Early Proterozoic.

Hence, the granites of Kanker pluton evolved in a transitional geodynamic environment involving the subduction and collision during the Archean-Proterozoic transition. The proposed geodynamic environment can explain the origin of the Dongargarh and Malanjkhand granites, and also account for the mineralization associated with the latter. Compositional variations of the Kanker granites are attributed to variable crust-mantle interactions. Precise age and isotopic data will provide better clues on the sequence of emplacement of these granite types, constraining the sources and the extent of interactions between them. With these limitations, a craton scale geological model is beyond the scope of this contribution.

CONCLUSIONS

- Kanker granites are geochemically classified into sanukitoids, biotite and two-mica granites and hybrid granites.
- Two discrete end-member sources, i.e., the enriched mantle and an older felsic crust, and their variable interactions are responsible for the compositional diversity of the Kanker granites.
- The evolution of the Kanker granites can be accounted for a transitional geodynamic environment, involving subduction and collisional tectonics during the Archean-Proterozoic transition.
- The collisional tectonic regime can also be related to the porphyry mineralization in the Malanjkhand granite and the A_2 affinity of the Dongargarh granite.

DATA AVAILABILITY STATEMENT

All datasets generated for this study are included in the article/supplementary material.

AUTHOR CONTRIBUTIONS

AA: field work and initial draft preparation. RE: field work, petrography, geochemical analysis, and data processing. NV: field work and petrography. KH: field work and petrography. MR: conceptualisaion of problem, field work, data interpretation, and supervision. All authors have contributed equally to the data interpretation and writing of the paper.

FUNDING

INDEX project (CSIR-NGRI).

ACKNOWLEDGMENTS

The authors thank Director, CSIR-NGRI, for the permission to publish this work, which is an outcome of the INDEX project (NGRI/Lib/2020/Pub-31). This study forms part of the Ph.D. thesis of RE. We are grateful to Steven Denyszyn for efficient editorial handling. Critical reviews by two reviewers helped to significantly improve the earlier version. Drs. M. Satyanarayanan and A. Keshav Krishna are acknowledged for providing the whole-rock major and trace elemental data.

REFERENCES

Ahmad, T., Kaulina, T. V., Wanjari, N., Mishra, M. K., and Nitkina, E. A. (2009). "U–Pb zircon chronology and Sm–Nd isotopic characteristics of the Amgaon and Tirodi Gneissic Complex, Central Indian Shield: constraints on Precambrian crustal evolution," in *Precambrian Continental Growth And Tectonism*, eds V. K. Singh, and R. Chandra (New Delhi: Excel India Publishers), 137–138.

Asthana, D., Kumar, H., Balakrishnan, S., Xia, Q., and Feng, M. (2016). An early cretaceous analogue of the ∼2.5 Ga Malanjkhand porphyry Cu deposit, Central India. *Ore Geol. Rev*. 72, 1197–1212. doi: 10.1016/j.oregeorev.2015.10.015

Asthana, D., Kumar, S., Vind, A. K., Zehra, F., Kumar, H., and Pophare, A. M. (2018). Geochemical fingerprinting of ∼2.5 Ga forearc-arc-backarc related magmatic suites in the Bastar Craton, central India. *J. Asian Earth Sci*. 157, 218–234. doi: 10.1016/j.jseaes.2017.10.006

Bhowmik, S. K., Wilde, S. A., and Bhandari, A. (2011). Zircon U-Pb/Lu-Hf and monazite chemical dating of the Tirodi biotite gneiss: implication for latest Palaeoproterozoic to Early Mesoproterozoic orogenesis in the Central Indian Tectonic Zone. *Geol. J*. 46, 574–596. doi: 10.1002/gj.1299

Bickford, M. E., Basu, A., Kamenov, G. D., Mueller, P. A., Patranabis-Deb, S., and Mukherjee, A. (2014). Petrogenesis of 1000 Ma felsic tuffs, Chhattisgarh and Indravati basins, Bastar craton, India: geochemical and Hf isotope constraints. *J. Geol*. 122, 43–54. doi: 10.1086/674802

Bonin, B. (2004). Do coeval mafic and felsic magmas in post-collisional to within-plate regimes necessarily imply two contrasting, mantle and crustal, sources? a review. *Lithos* 78, 1–24. doi: 10.1016/j.lithos.2004.04.042

Bonin, B. (2007). A-type granites and related rocks: evolution of a concept, problems and prospects. *Lithos* 97, 1–29. doi: 10.1016/j.lithos.2006.12.007

Cawood, P. A., Hawkesworth, C. J., and Dhuime, B. (2013). The continental record and the generation of continental crust. *Bull. Geol. Soc. Am*. 125, 14–32. doi: 10.1130/B30722.1

Condie, K. C., and Kröner, A. (2008). When did plate tectonics begin? evidence from the geologic record. *Spec. Pap. Geol. Soc. Am*. 440, 281–294. doi: 10.1130/2008.2440(14)

Deshpande, G. G., Mohabey, N. K., and Deshpande, M. S. (1990). Petrography and tectonic setting of Dongargarh volcanics. *Visesa Prakasana-Bharatiya Bhuvaijñanika Sarveksana* 260–286.

Dhuime, B., Hawkesworth, C. J., Cawood, P. A., and Storey, C. D. (2012). A change in the geodynamics of continental growth 3 billion years ago. *Science* 335, 1334–1336. doi: 10.1126/science.1216066

Duggen, S., Portnyagin, M., Baker, J., Ulfbeck, D., Hoernle, K., Garbe-Schönberg, D., et al. (2007). Drastic shift in lava geochemistry in the volcanic-front to rear-arc region of the Southern Kamchatkan subduction zone: evidence for the transition from slab surface dehydration to sediment melting. *Geochim. Cosmochim. Acta* 71, 452–480. doi: 10.1016/j.gca.2006.09.018

Durrheim, R. J., and Mooney, W. D. (1991). Archean and Proterozoic crustal evolution: evidence from crustal seismology. *Geology* 19, 606–609. doi: 10.1130/0091-7613(1991)019<0606:AAPCEE>2.3.CO;2

Eby, G. N. (1992). Chemical subdivision of the A-type granitoids: petrogenetic and tectonic implications. *Geology* 20, 641–644. doi: 10.1130/0091-7613(1992)020<0641:CSOTAT>2.3.CO;2

Elangovan, R., Asokan, A. D., Pandit, D., and Ram Mohan, M. (2020). Magma chamber processes and geodynamic implications of the Pithora pluton, Bastar Craton, Central India. *Geol. J*. 55, 2738–2759. doi: 10.1002/gj.3534

Elangovan, R., Krishna, K., Vishwakarma, N., Hari, K. R., and Mohan, M. R. (2017). Interaction of coeval felsic and mafic magmas from the Kanker granite, Pithora region, Bastar Craton, Central India. *J. Earth Syst. Sci*. 126:92. doi: 10.1007/s12040-017-0886-z

Elliott, T. (2004). Tracers of the slab. *Geophys. Monogr. Ser*. 138, 23–45. doi: 10.1029/138GM03

French, J. E., Heaman, L. M., Chacko, T., and Srivastava, R. K. (2008). 1891–1883 Ma Southern Bastar–Cuddapah mafic igneous events, India: a newly recognized large igneous province. *Precambrian Res*. 160, 308–322. doi: 10.1016/j.precamres.2007.08.005

Ghosh, J. G. (2004). 3.56 Ga tonalite in the central part of the Bastar craton, India: oldest Indian date. *J. Asian Earth Sci*. 23, 359–364. doi: 10.1016/S1367-9120(03)00136-6

Halla, J. (2005). Late Archean high-Mg granitoids (sanukitoids) in the southern Karelian domain, eastern Finland: Pb and Nd isotopic constraints on crust-mantle interactions. *Lithos* 79, 161–178. doi: 10.1016/j.lithos.2004.05.007

Halla, J., van Hunen, J., Heilimo, E., and Hölttä, P. (2009). Geochemical and numerical constraints on Neoarchean plate tectonics. *Precambrian Res*. 174, 155–162. doi: 10.1016/j.precamres.2009.07.008

Harris, N. B. W., and Inger, S. (1992). Trace element modelling of pelite-derived granites. *Contrib. Mineral. Petrol*. 110, 46–56. doi: 10.1007/BF00310881

Harris, N. B. W., Pearce, J. A., and Tindle, A. G. (1986). Geochemical characteristics of collision-zone magmatism. *Geol. Soc. Spec. Publ*. 19, 67–81. doi: 10.1144/GSL.SP.1986.019.01.04

Hawkesworth, C. J., Turner, S. P., McDermott, F., Peate, D. W., and Van Calsteren, P. (1997). U-Th isotopes in arc magmas: implications for element transfer from the subducted crust. *Science* 276, 551–555. doi: 10.1126/science.276.5312.551

Heilimo, E., Halla, J., and Hölttä, P. (2010). Discrimination and origin of the sanukitoid series: geochemical constraints from the Neoarchean western Karelian Province (Finland). *Lithos* 115, 27–39. doi: 10.1016/j.lithos.2009.11.001

Hopkinson, T. N., Harris, N. B. W., Warren, C. J., Spencer, C. J., Roberts, N. M. W., Horstwood, M. S. A., et al. (2017). The identification and significance of pure sediment-derived granites. *Earth Planet. Sci. Lett*. 467, 57–63. doi: 10.1016/j.epsl.2017.03.018

Hou, Z., and Cook, N. J. (2009). Metallogenesis of the Tibetan collisional orogen: a review and introduction to the special issue. *Ore Geol. Rev*. 36, 2–24. doi: 10.1016/j.oregeorev.2009.05.001

Hussain, M. F., Mondal, M. E. A., and Ahmad, T. (2004). Petrological and geochemical characteristics of Archean gneisses and granitoids from Bastar Craton, Central India - Implication for subduction related magmatism. *Gondwana Res*. 7, 531–537. doi: 10.1016/S1342-937X(05)70803-0

Janoušek, V., Moyen, J.-F., Martin, H., Erban, V., and Farrow, C. (2016). *Geochemical Modelling of Igneous Processes–Principles and Recipes in R Language*. Berlin: Springer.

Jayananda, M., Dey, S., and Aadhiseshan, K. R. (2020). "Evolving early earth: Insights from peninsular India," in *Geodynamics of the Indian Plate: Evolutionary Perspectives*, eds. N. Gupta and S. K. Tandon (Cham: Springer International Publishing), 5–103. doi: 10.1007/978-3-030-15989-4_2

Keller, C. B., and Schoene, B. (2012). Statistical geochemistry reveals disruption in secular lithospheric evolution about 2.5Gyr ago. *Nature* 485, 490–493. doi: 10.1038/nature11024

Khanna, T. C., Bizimis, M., Barbeau, D. L., Keshav Krishna, A., and Sesha Sai, V. V. (2019). Evolution of ca. 2.5 Ga dongargarh volcano-sedimentary supergroup, Bastar craton, Central India: constraints from zircon U-Pb geochronology, bulk-rock geochemistry and Hf-Nd isotope systematics. *Earth Sci. Rev*. 190, 273–309. doi: 10.1016/j.earscirev.2018.11.014

Krishna, A. K., Khanna, T. C., and Mohan, K. R. (2016). Rapid quantitative determination of major and trace elements in silicate rocks and soils employing fused glass discs using wavelength dispersive X-ray fluorescence spectrometry. *Spectrochim. Acta B At. Spectrosc*. 122, 165–171. doi: 10.1016/j.sab.2016.07.004

La Flèche, M. R., Camire, G., and Jenner, G. A. (1998). Geochemistry of post-Acadian, Carboniferous continental intraplate basalts from the Maritimes Basin, Magdalen islands, Quebec, Canada. *Chem. Geol*. 148, 115–136. doi: 10.1016/S0009-2541(98)00002-3

Laurent, O., Martin, H., Doucelance, R., Moyen, J. F., and Paquette, J. L. (2011). Geochemistry and petrogenesis of high-K "sanukitoids" from the Bulai pluton, Central Limpopo Belt, South Africa: implications for geodynamic changes at the Archaean-Proterozoic boundary. *Lithos* 123, 73–91. doi: 10.1016/j.lithos.2010.12.009

Laurent, O., Martin, H., Moyen, J. F., and Doucelance, R. (2014). The diversity and evolution of late-Archean granitoids: evidence for the onset of "modern-style" plate tectonics between 3.0 and 2.5 Ga. *Lithos* 205, 208–235. doi: 10.1016/j.lithos.2014.06.012

Le Maitre, R. W (1989). *A Classification of Igneous Rocks and Glossary of Terms: Recommendations of the International Union of Geological Sciences and Submissions on the Systematics of Igneous Rocks*. Oxford: Blackwell Scientific Publications. p. 193.

Lee, C. T. A., Yeung, L. Y., McKenzie, N. R., Yokoyama, Y., Ozaki, K., and Lenardic, A. (2016). Two-step rise of atmospheric oxygen linked to the growth of continents. *Nat. Geosci*. 9, 417–424. doi: 10.1038/ngeo2707

Liao, A. C. Y., Shellnutt, J. G., Hari, K. R., Denyszyn, S. W., Vishwakarma, N., and Verma, C. B. (2019). A petrogenetic relationship between 2.37 Ga boninitic dyke swarms of the Indian Shield: evidence from the Central Bastar Craton and the NE Dharwar Craton. *Gondwana Res*. 69, 193–211. doi: 10.1016/j.gr.2018.12.007

Manikyamba, C., Santosh, M., Kumar, B. C., Rambabu, S., Tang, L., Saha, A., et al. (2016). Zircon U-Pb geochronology, Lu-Hf isotope systematics, and geochemistry of bimodal volcanic rocks and associated granitoids from Kotri Belt, Central India: implications for Neoarchean–Paleoproterozoic crustal growth. *Gondwana Res*. 38, 313–333. doi: 10.1016/j.gr.2015.12.008

Manu Prasanth, M. P., Hari, K. R., Chalapathi Rao, N. V., Hou, G., and Pandit, D. (2018). An island-arc tectonic setting for the Neoarchean Sonakhan Greenstone Belt, Bastar Craton, Central India: Insights from the chromite mineral chemistry and geochemistry of the siliceous high-Mg basalts (SHMB). *Geol. J*. 53, 1526–1542. doi: 10.1002/gj.2971

Manu Prasanth, M. P., Hari, K. R., Chalapathi Rao, N. V., Santosh, M., Hou, G., Tsunogae, T., et al. (2019). Neoarchean suprasubduction zone magmatism in the Sonakhan greenstone belt, Bastar Craton, India: implications for subduction initiation and melt extraction. *Geol. J*. 54, 3980–4000. doi: 10.1002/gj.3398

Martin, H., Moyen, J. F., and Rapp, R. (2009). The sanukitoid series: magmatism at the archaean-proterozoic transition. *Earth Environ. Sci. Trans. R. Soc. Edinburgh*. 100, 15–33. doi: 10.1017/S1755691009016120

Meert, J. G., Pandit, M. K., Pradhan, V. R., Banks, J., Sirianni, R., Stroud, M., et al. (2010). Precambrian crustal evolution of Peninsular India: a 3.0-billion-year odyssey. *J. Asian Earth Sci*. 39, 483–515. doi: 10.1016/j.jseaes.2010.04.026

Mikkola, P., Huhma, H., Heilimo, E., and Whitehouse, M. (2011). Archean crustal evolution of the Suomussalmi district as part of the Kianta Complex, Karelia: constraints from geochemistry and isotopes of granitoids. *Lithos* 125, 287–307. doi: 10.1016/j.lithos.2011.02.012

Mohan, M. R., Asokan, A. D., and Wilde, S. A. (2019). Crustal growth of the Eastern Dharwar Craton: a Neoarchean collisional orogeny? *Geol. Soc. London Spec. Publ*. SP489-2019–108. doi: 10.1144/SP489-2019-108

Mohanty, S. P. (2015). Palaeoproterozoic supracrustals of the Bastar Craton: dongargarh supergroup and sausar group. *Geol. Soc. Mem*. 43, 151–164. doi: 10.1144/M43.11

Mondal, M. E. A., Hussain, M. F., and Ahmad, T. (2006). Continental growth of Bastar craton, Central Indian shield during precambrian via multiphase subduction and lithospheric extension/rifting: evidence from geochemistry of gneisses, granitoids and mafic dykes. *J. Geosci*. 49, 137–151.

Mondal, M. E. A., Hussain, M. F., and Ahmad, T. (2019). Archean granitoids of the Bastar Craton, Central India. *Geol. Soc. London Spec. Publ*. SP489-2019–311. doi: 10.1144/SP489-2019-311

Moyen, J. F., and Laurent, O. (2018). Archaean tectonic systems: a view from igneous rocks. *Lithos* 302–303, 99–125. doi: 10.1016/j.lithos.2017.11.038

Moyen, J. F., Laurent, O., Chelle-Michou, C., Couzinié, S., Vanderhaeghe, O., Zeh, A., et al. (2017). Collision vs. subduction-related magmatism: two contrasting ways of granite formation and implications for crustal growth. *Lithos* 277, 154–177. doi: 10.1016/j.lithos.2016.09.018

Moyen, J. F., Martin, H., Jayananda, M., and Auvray, B. (2003). Late archaean granites: a typology based on the Dharwar Craton (India). *Precambrian Res*. 127, 103–123. doi: 10.1016/S0301-9268(03)00183-9

Narayana, B. L., Mallikharjuna Rao, J., Subba Rao, M. V., Murthy, N. N., and Divakara Rao, V. (2000). Geochemistry and origin of early proterozoic Dongargarh Rapakivi Granite Complex, Central India - an

example for magma mixing and differentiation. *Gondwana Res.* 3, 507–520. doi: 10.1016/S1342-937X(05)70757-7

O'Connor, J. T. (1965). A classification for quartz-rich igneous rocks. *Geol. Surv. Prof. Pap*. 525:79.

Pandit, D., and Panigrahi, M. K. (2012). Comparative petrogenesis and tectonics of Paleoproterozoic Malanjkhand and Dongargarh granitoids, Central India. *J. Asian Earth Sci*. 50, 14–26. doi: 10.1016/j.jseaes.2012.01.017

Panigrahi, M. K., Bream, B. R., Misra, K. C., and Naik, R. K. (2004). Age of granitic activity associated with copper–molybdenum mineralization at Malanjkhand, Central India. *Miner. Depos*. 39, 670–677. doi: 10.1007/s00126-004-0441-0

Pearce, J. A., Harris, N. B. W., and Tindle, A. G. (1984). Trace element discrimination diagrams for the tectonic interpretation of granitic rocks. *J. Petrol*. 25, 956–983. doi: 10.1093/petrology/25.4.956

Rajesh, H. M., Mukhopadhyay, J., Beukes, N. J., Gutzmer, J., Belyanin, G. A., and Armstrong, R. A. (2009). Evidence for an early Archaean granite from Bastar craton, India. *J. Geol. Soc. London*. 166, 193–196. doi: 10.1144/0016-76492008-089

Ramakrishnan, M. (1990). Crustal development in southern Bastar central Indian craton. *Visesa Prakasana-Bharatiya Bhuvaijñanika Sarveksana* 44–66.

Rapp, R. P., Shimizu, N., Norman, M. D., and Applegate, G. S. (1999). Reaction between slab-derived melts and peridotite in the mantle wedge: experimental constraints at 3.8 GPa. *Chem. Geol*. 160, 335–356. doi: 10.1016/S0009-2541(99)00106-0

Reimink, J. R., Chacko, T., Stern, R. A., and Heaman, L. M. (2016). The birth of a cratonic nucleus: lithogeochemical evolution of the 4.02-2.94 Ga Acasta Gneiss Complex. *Precambrian Res*. 281, 453–472. doi: 10.1016/j.precamres.2016.06.007

Roy, A., Kagami, H., Yoshida, M., Roy, A., Bandyopadhyay, B. K., and Chattopadhyay, A. (2006). Rb–Sr and Sm–Nd dating of different metamorphic events from the sausar mobile belt, central India: implications for proterozoic crustal evolution. *J. Asian Earth Sci*. 26, 61–76. doi: 10.1016/j.jseaes.2004.09.010

Santosh, M., Hari, K. R., He, X. F., Han, Y. S., and Manu Prasanth, M. P. (2018). Oldest lamproites from Peninsular India track the onset of Paleoproterozoic plume-induced rifting and the birth of Large Igneous Province. *Gondwana Res.* 55, 1–20. doi: 10.1016/j.gr.2017.11.005

Santosh, M., Tsunogae, T., Yang, C. X., Han, Y. S., Hari, K. R., Prasanth, M. P. M., et al. (2020). The Bastar craton, central India: a window to Archean – Paleoproterozoic crustal evolution. *Gondwana Res*. 79, 157–184. doi: 10.1016/j.gr.2019.09.012

Sarkar, G., Corfu, F., Paul, D. K., McNaughton, N. J., Gupta, S. N., and Bishui, P. K. (1993). Early Archean crust in Bastar Craton, Central India-a geochemical and isotopic study. *Precambrian Res*. 62, 127–137. doi: 10.1016/0301-9268(93)90097-L

Satyanarayanan, M., Balaram, V., Sawant, S. S., Subramanyam, K. S. V., Krishna, G. V., Dasaram, B., et al. (2018). Rapid determination of REEs, PGEs, and other trace elements in geological and environmental materials by high resolution inductively coupled plasma mass spectrometry. *At. Spectrosc*. 39, 1–15.

Shand, S. J. (1943). *The Eruptive Rocks*. New York, NY: John Wiley Publishers. p. 444.

Shirey, S. B., and Hanson, G. N. (1984). Mantle-derived Archaean monozodiorites and trachyandesites. *Nature* 310, 222–224. doi: 10.1038/310222a0

Sillitoe, R. H. (2010). Porphyry copper systems. *Econ. Geol*. 105, 3–41. doi: 10.2113/gsecongeo.105.1.3

Sizova, E., Gerya, T., Brown, M., and Perchuk, L. L. (2010). Subduction styles in the Precambrian: insight from numerical experiments. *Lithos* 116, 209–229. doi: 10.1016/j.lithos.2009.05.028

Smithies, R. H., and Champion, D. C. (2000). The Archaean high-Mg diorite suite: links to tonalite–trondhjemite–granodiorite magmatism and implications for early Archaean crustal growth. *J. Petrol*. 41, 1653–1671. doi: 10.1093/petrology/41.12.1653

Srivastava, R. K., Singh, R. K., and Verma, S. P. (2004). Neoarchaean mafic volcanic rocks from the southern Bastar greenstone belt, Central India: petrological and tectonic significance. *Precambrian Res*. 131, 305–322. doi: 10.1016/j.precamres.2003.12.013

Steenfelt, A., Garde, A. A., and Moyen, J. F. (2005). Mantle wedge involvement in the petrogenesis of Archaean gray gneisses in West Greenland. *Lithos* 79, 207–228. doi: 10.1016/j.lithos.2004.04.054

Stein, H. J., Hannah, J. L., Zimmerman, A., Markey, R. J., Sarkar, S. C., and Pal, A. B. (2004). A 2.5 Ga porphyry Cu-Mo-Au deposit at Malanjkhand, central India: Implications for Late Archean continental assembly. *Precambrian Res*.134,189–226. doi: 10.1016/j.precamres.2004.05.012

Sun, S.-S., and McDonough, W. F. (1989). Chemical and isotopic systematics of oceanic basalts: implications for mantle composition and processes. *Geol. Soc. London Spec. Publ*. 42, 313–345. doi: 10.1144/GSL.SP.1989.042.01.19

Sylvester, P. J. (1998). Post-collisional strongly peraluminous granites. *Lithos* 45, 29–44. doi: 10.1016/S0024-4937(98)00024-3

Woodhead, J. D., Hergt, J. M., Davidson, J. P., and Eggins, S. M. (2001). Hafnium isotope evidence for "conservative" element mobility during subduction zone processes. *Earth Planet. Sci. Lett*. 192, 331–346. doi: 10.1016/S0012-821X(01)00453-8

Conflict of Interest: The authors declare that the research was conducted in the absence of any commercial or financial relationships that could be construed as a potential conflict of interest.

The handling editor declared a past co-authorship with one of the authors NV.